J. Fluid Mech. (2010), *vol.* 665, *pp.* 300–333.
doi:10.1017/S002211201000399X

Heat transport and the large-scale circulation in rotating turbulent Rayleigh–Bénard convection

JIN-QIANG ZHONG AND GUENTER AHLERS†

Department of Physics, University of California, Santa Barbara, CA 93106, USA

(Received 6 May 2010; revised 20 July 2010; accepted 20 July 2010;
first published online 26 October 2010)

Measurements of the Nusselt number Nu and of properties of the large-scale circulation (LSC) for turbulent Rayleigh–Bénard convection are presented in the presence of rotation about a vertical axis at angular speeds $0 \leqslant \Omega \lesssim 2\,\mathrm{rad\,s^{-1}}$. The sample chamber was cylindrical with a height equal to the diameter, and the fluid contained in it was water. The LSC was studied by measuring sidewall temperatures as a function of azimuthal position. The measurements covered the Rayleigh-number range $3 \times 10^8 \lesssim Ra \lesssim 2 \times 10^{10}$, the Prandtl-number range $3.0 \lesssim Pr \lesssim 6.4$ and the Rossby-number range $0 \leqslant (1/Ro \propto \Omega) \lesssim 20$. At modest $1/Ro$, we found an enhancement of Nu due to Ekman-vortex pumping by as much as 20 %. As $1/Ro$ increased from zero, this enhancement set in discontinuously at and grew above $1/Ro_c$. The value of $1/Ro_c$ varied from about 0.48 at $Pr = 3$ to about 0.35 at $Pr = 6.2$. At sufficiently large $1/Ro$ (large rotation rates), Nu decreased again, due to the Taylor–Proudman (TP) effect, and reached values well below its value without rotation. The maximum enhancement increased with increasing Pr and decreasing Ra and, we believe, was determined by a competition between the Ekman enhancement and the TP depression. The temperature signature along the sidewall of the LSC was detectable by our method up to $1/Ro \simeq 1$. The frequency of cessations α of the LSC grew dramatically with increasing $1/Ro$, from about $10^{-5}\,\mathrm{s^{-1}}$ at $1/Ro = 0$ to about $2 \times 10^{-4}\,\mathrm{s^{-1}}$ at $1/Ro = 0.25$. A discontinuous further increase of α, by about a factor of 2.5, occurred at $1/Ro_c$. With increasing $1/Ro$, the time-averaged and azimuthally averaged vertical thermal gradient along the sidewall first decreased and then increased again, with a minimum somewhat below $1/Ro_c$. The Reynolds number of the LSC, determined from oscillations of the time correlation functions of the sidewall temperatures, was constant within our resolution for $1/Ro \lesssim 0.3$ and then decreased with increasing $1/Ro$. The retrograde rotation rate of the LSC circulation plane exhibited complex behaviour as a function of $1/Ro$ even at small rotation rates corresponding to $1/Ro < 1/Ro_c$.

Key words: Bénard convection, rotating turbulence, turbulent convection

1. Introduction

Understanding turbulent convection in a fluid confined between two horizontal plates and heated from below (Rayleigh–Bénard convection (RBC); for reviews, see e.g. Kadanoff 2001; Ahlers, Grossmann & Lohse 2002, 2009; Ahlers 2009; Lohse & Xia 2010) remains one of the challenging problems in nonlinear physics.

† Email address for correspondence: guenter@physics.ucsb.edu

It is well established that a major component of the dynamics of this system is a large-scale circulation (LSC). For a cylindrical system of height L, which is almost equal to diameter D (aspect ratio $\Gamma \equiv L/D \simeq 1$), the LSC takes the form of a single convection roll. It has some particularly interesting properties. The dynamics of its near-vertical circulation plane can be described well as a stochastically driven system, with the driving due to the smaller scales of the turbulent flow (Brown & Ahlers 2007*a*, 2008*b*). Most of the time, the orientation of the circulation plane undergoes azimuthal diffusion (Sun, Xi & Xia 2005; Xi, Zhou & Xia 2006; Brown & Ahlers 2006*a*,*b*). In addition, it has a number of interesting features, including torsional oscillations (Funfschilling & Ahlers 2004; Funfschilling, Brown & Ahlers 2008), a 'sloshing' mode (Brown & Ahlers 2009; Xi *et al.* 2009; Zhou *et al.* 2009) and sudden rotations of the azimuthal orientation (Cioni, Ciliberto & Sommeria 1997; Brown & Ahlers 2006*b*). Occasionally, there are cessations of the circulation (where the flow stops completely), followed by a re-birth of the circulation at a random new orientation (Brown, Nikolaenko & Ahlers 2005*a*; Brown & Ahlers 2006*b*). All of these features are explained well by the stochastic model of Brown & Ahlers (2007*a*, 2008*b*).

A second important aspect is the existence of thin thermal and viscous boundary layers (BLs) just above the bottom and just below the top plate. Even when the interior of the system is highly turbulent, these BLs, although fluctuating in time, are laminar (Zhou & Xia 2010) and can be described well by the classical Prandtl–Blasius boundary-layer theory. The thermal BLs control the global heat transport of the system (Ciliberto, Cioni & Laroche 1996; Ahlers, Brown & Nikolaenko 2006*b*). The heat transport is usually expressed in terms of the ratio of the effective thermal conductivity of the convecting fluid to the diffusive thermal conductivity λ of the quiescent fluid known as the Nusselt number:

$$Nu = \frac{QL}{A\Delta T\lambda}. \tag{1.1}$$

Here Q is the heat current carried by the fluid, A is the cross-sectional area of the sample, L is the sample height and ΔT is the applied temperature difference. For a reasonable approximation, about half of ΔT is found across each thermal BL, and the sample interior, on average, is nearly isothermal (see e.g. Brown & Ahlers (2007*b*) and §4). Over the parameter range of interest for the present work, the dependence of Nu on the Rayleigh number

$$Ra \equiv \frac{\alpha g \Delta T L^3}{\kappa \nu} \tag{1.2}$$

(α is the isobaric thermal expansion coefficient, g is the acceleration of gravity, κ is the thermal diffusivity and ν is the kinematic viscosity) and on the Prandtl number

$$Pr \equiv \nu/\kappa \tag{1.3}$$

is explained rather well by the model of Grossmann and Lohse (GL) (Grossmann & Lohse 2000, 2001).

In the present paper, we address the question of how the LSC and the heat transport are modified when the sample is rotated about a vertical axis. The influence of the Coriolis force due to rotation is of importance in numerous astrophysical and geophysical phenomena, including convection in the Arctic and Antarctic oceans (see e.g. Marshall & Schott 1999; Gascard *et al.* 2002), Earth's outer core (see e.g. Glatzmaier *et al.* 1999; Jones 2000), the interior of gaseous giant planets (see e.g. Busse 1994) and the outer layer of the Sun (see e.g. Miesch 2000).

A lot of experimental, numerical and theoretical work has been carried out before on RBC in the presence of rotation. Early linear stability analysis (see e.g. Chandrasekhar 1981) revealed that the Coriolis force has a stabilizing influence on the conduction state. This is understood on the basis of the Taylor–Proudman (TP) effect (see e.g. Tritton 1988), which implies that convective heat transport parallel to the rotation axis tends to be suppressed. Interesting phenomena involving the influence of rotation on pattern formation have been observed and studied close to but above the onset of convection by many authors, including Veronis (1966, 1968), Küppers & Lortz (1969), Küppers (1970), Clever & Busse (1979), Heikes & Busse (1980), Busse & Heikes (1980), Lucas, Pfotenhauer & Donnelly (1983), Buell & Catton (1983), Pfotenhauer, Lucas & Donnelly (1984), Niemela & Donnelly (1986), Pfotenhauer, Niemela & Donnelly (1987), Bodenschatz *et al.* (1992), Ecke, Zhong & Knobloch (1992), Fantz *et al.* (1992), Tu & Cross (1992), Zhong, Ecke & Steinberg (1993), Ning & Ecke (1993*a*, *b*), Neufeld, Friedrich & Haken (1993), Hu, Ecke & Ahlers (1995, 1997), Millán-Rodríguez *et al.* (1995), Liu & Ecke (1997*a*, 1999), Ponty, Passot & Sulem (1997), Bajaj *et al.* (1998), Hu *et al.* (1998), Liu & Ecke (1999), Bajaj, Ahlers & Pesch (2002), Thompson, Bajaj & Ahlers (2002), Choi *et al.* (2004), Sánchez-Álvarez *et al.* (2005), Becker *et al.* (2006), Becker & Ahlers (2006*a*, *b*), Rubio, Lopez & Marques (2010) and Scheel, Mutyaba & Kimmel (2010).

In the present paper, we focus on a parameter range well above onset, where the interior of the RBC system is turbulent. Much prior work exists as well in this regime. In a previous paper, Brown & Ahlers (2006*a*) discussed the very weak influence of Earth's rotation on the LSC in turbulent RBC. Here we study the effect of deliberate rotation about a vertical axis. It is worth noting that any rotation frequency f imposed in the laboratory (which typically will be larger than 10^{-3} Hz or so) will be two or more orders of magnitude larger than the Earth's rotation rate of about 10^{-5} Hz. The effect of deliberate rotation has been investigated before by numerous experiments, including those of Rossby (1969), Boubnov & Golitsyn (1986), Boubnov & Golitsyn (1990), Fernando, Chen & Boyer (1991), Zhong *et al.* (1993), Liu & Ecke (1997*b*), Sakai (1997), Vorobieff & Ecke (1998), Hart & Olsen (1999), Hart, Kittelman & Ohlsen (2002), Vorobieff & Ecke (2002), Kunnen, Clercx & Geurts (2008*a*, *b*), Zhong *et al.* (2009), Stevens *et al.* (2009), Liu & Ecke (2009), King *et al.* (2009), Kunnen, Geurts & Clercx (2010) and Niemela, Babuin & Sreenivasan (2010). It has also been studied, by using direct numerical simulations (DNS), by Julin *et al.* (1996*a*, *b*), Kunnen, Clercx & Geurts (2006, 2008*b*), Zhong *et al.* (2009), Stevens *et al.* (2009), Schmitz & Tilgner (2009), King *et al.* (2009), Kunnen *et al.* (2010), Mishra *et al.* (2010) and Stevens, Clercx & Lohse (2010*a*, *b*). For a summary of much of this work, we refer the reader, for instance, to the more detailed introduction of the recent paper by Kunnen *et al.* (2010). The relationship of our work to some of this sizable literature will be discussed in § 6.

Here we report on an experimental study of a cylindrical sample with aspect ratio $\Gamma \simeq 1$ as a function of the rotation rate $\Omega = 2\pi f$ (f is the rotation frequency in Hz) over the ranges $3 \times 10^8 \lesssim Ra \lesssim 2 \times 10^{10}$ and $3.0 \lesssim Pr \lesssim 6.4$. The dimensionless rotation rates are expressed in various forms in the literature, including the Ekman number

$$Ek = \frac{\nu}{L^2} \cdot \frac{1}{\Omega}, \tag{1.4}$$

the convective Rossby number (henceforth simply referred to as the Rossby number, but distinct from the inertial Rossby number, which will not appear in this paper;

Run	T_m (°C)	ΔT (K)	Pr	$10^{-9}Ra$	$Ro\ \Omega$	$10^{5}Ek\ \Omega$	$10^{-10}Ta/\Omega^2$
E1	23.00	4.68	6.41	1.21	0.1048	1.527	1.716
E2	24.00	0.996	6.26	0.273	0.0493	1.494	1.793
E3	24.00	7.96	6.26	2.19	0.1396	1.494	1.793
E4	40.00	0.996	4.38	0.563	0.0618	1.091	3.364
E5	40.00	1.99	4.38	1.13	0.0875	1.090	3.364
E6	40.00	3.98	4.38	2.25	0.1236	1.090	3.364
E7	40.00	15.87	4.38	8.97	0.2467	1.090	3.364
E8	40.00	31.69	4.38	17.91	0.3486	1.090	3.364
E9	50.00	5.96	3.62	4.61	0.1642	0.921	4.715
E10	60.00	1.21	3.05	1.22	0.0789	0.790	6.414
E11	60.00	7.93	3.05	7.99	0.2021	0.790	6.414

TABLE 1. Parameters for all experimental runs. The last three columns give the products $(Ro\ \Omega)$ (rad s^{-1}), $(Ek\ \Omega)$ (rad s^{-1}) and $(Ta\ \Omega^{-2})$ (s^2 rad^{-2}), which are constant material parameters for a given experimental run.

see e.g. Tritton 1988)

$$Ro = \frac{\sqrt{\alpha g \Delta T / L}}{2\Omega}, \tag{1.5}$$

and the Taylor number

$$Ta = \left(\frac{L^2}{\nu} \cdot 2\Omega\right)^2 = \left(\frac{2}{Ek}\right)^2. \tag{1.6}$$

Most of our measurements were done at several constant Pr and Ra, varying Ω (see table 1). We find that the observed phenomena are best described by using Ro, but prefer to use its inverse $1/Ro$ in order to have a parameter proportional to the rotation rate. Our measurements extend from $1/Ro = 0$ (no rotation) to $1/Ro \simeq 20$. More information about various parameter ranges is reported in table 1. We report results for the Nusselt number, as well as for the effect of rotation on properties of the LSC. Some of our results have been reported briefly before (Stevens *et al.* 2009; Zhong *et al.* 2009) in two publications that described the results of a very fruitful collaboration with the groups of H. J. H. Clercx and D. Lohse, who carried out DNS of this system over parameter ranges that overlapped with ours and revealed excellent agreement with the experiment.

We (as well as others) found that modest rotation enhances the heat transport in this system due to Ekman-vortex pumping, but that strong rotation decreases the Nusselt number. The decrease is usually attributed to the Taylor–Proudman 'theorem' (Tritton 1988), which states that velocity gradients parallel to the rotation axis, and thus also the convected heat transport, are suppressed. We remark that strictly this 'theorem' is valid only when nonlinear, dissipative and buoyancy terms are absent in the equation of motion. When the Coriolis force is much larger than the inertial and buoyancy forces as represented by the nonlinear and buoyancy terms in the Boussinesq equation, then $1/Ro$ (as well as the inverse inertial Rossby number) is much greater than one. When the dissipative term is also much less than the Coriolis term, then $1/Ek \gg 1$. When all of those conditions pertain, then the TP 'theorem' becomes a good approximation and the phenomenon dominates; but since the 'theorem' is no longer exact, we prefer to refer to the phenomenon as the TP 'effect'. This effect is also present at modest rotation, but there it does not dominate. Our Nusselt-number

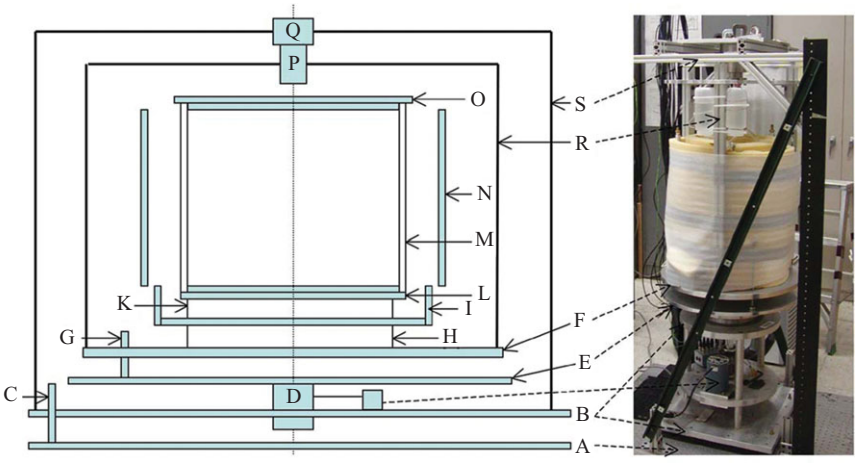

FIGURE 1. (Colour online) Schematic diagram and photograph of the apparatus. For an identification of the various components, see § 2.1.

measurements, shown below in figures 4, 8 and 20, indicate for instance that for $Pr \simeq 4.4$ the TP effect can become noticeable when $1/Ro \simeq 2$; for $Pr \simeq 6.3$ it shows up measurably only when $1/Ro \simeq 7$. When the strength of the TP effect increases to the point where it dominates completely, then Nu is suppressed completely and the onset of convection is reached from above. As we shall see below in figure 9, none of the measurements in the current paper comes close to this latter condition.

In the next section, we describe the apparatus, experimental methods, and procedures in some detail. Section 2.1 discusses the construction of the rotating table and the sample that is mounted on it. The thermometry involved in our work is explained in § 2.2. In § 2.3, we give details of the general experimental protocol. Section 2.4 explains how high-precision Nusselt-number measurements were made. In § 2.5, we describe the sidewall temperature measurements that were used to obtain information about the LSC. Results for Nu are presented in § 3, first for $\Omega = 0$ and then for $\Omega > 0$. Measurements of the temperature gradient along the sidewall are presented in § 4. Several properties of the LSC are described in § 5. These include, in sequence, the associated Reynolds number Re, the time-averaged temperature amplitude $\langle \delta \rangle$, the size of the root-mean-square temperature fluctuations $\langle \delta T \rangle$ about a smooth azimuthal cosine variation, the occurrence of cessations and the dependence of the cessation frequency α on $1/Ro$, and various aspects of the retrograde rotation rate of the LSC circulation plane. A summary and discussion of the results is provided in § 6.

2. Experimental apparatus and methods

2.1. *The rotating table and the convection system*

A schematic diagram and a photograph of the apparatus are shown in figure 1. A heavy aluminum plate A rested securely on the laboratory floor. A second plate of size 50 cm × 50 cm was the base plate of the static support structure B of the rotating table (in the schematic only the plate is shown) and was supported on three equally spaced screws C (only one is shown). The screws were used to level the support structure B to within 10^{-4} rad. The rotation axis D of the table was accurately orthogonal to B and carried the rotating plate E. It was driven by a superior electric model M093-FC11 stepping motor operated in a microstepping mode. All other mechanical

details of the table construction are omitted here as they are not essential to the table performance. Supported by three further screws G was the base plate F of the convection system. This system was nearly the same as that described elsewhere (Brown *et al.* 2005*b*), and here we shall be brief. The screws G were used to ensure that the upper surface of the sample bottom plate L was level within 10^{-4} rad. Supported on F by a stainless-steel ring was a thermal shield I. The bottom of I was covered by a heater, and a thermistor was located at the centre of the upper surface of I. A second thermistor and heater were located near the periphery of I; unfortunately, insufficient electrical leads were available in the rotating frame to allow this extra thermal protection to be used during most of this project. This compromise did lead to a small deterioration in the accuracy of the Nusselt-number measurements, but did not affect the precision and thus had no influence on the ratios of Nu with and without rotation. In a later version of the apparatus, more electrical feed-throughs were installed and this auxiliary bottom-shield heater was put to use once more.

The copper bottom plate L was supported on a second stainless-steel ring K and had an anvil on its upper side that protruded into the Plexiglas sidewall M. Plate L had a heater covering its bottom surface as described before. The copper top plate O rested on and also protruded into the sidewall, and had in it a double-spiral water-cooling channel. The water circuit was brought into the rotating frame through the feed-through (P, Q). The rotor P of the feed-through was supported by a structure R from the rotating base plate F, and the stator Q was supported similarly via S from the stator plate B. A dual Dynamic Sealing Technologies model GP-321-E-ESM428 water feed-through (sufficient for a single water circuit) worked in conjunction with feed-throughs for electrical leads. Additional electrical feed-throughs were available at the bottom of the system through the rotation axis D. In a later version of the apparatus, the water feed-through was replaced by a quadruple Scott Rotary Seals model AP-341 four-passage feed-through, combined with an ES-12 slip ring for electrical leads. This unit could accommodate two water circuits. Both types of water feed-throughs were supposed to be suitable for use with water as the fluid, but after extended use began to leak because of corrosion and associated abrasion. Thus, in a later version of the apparatus, we used the Scott Rotary Seals unit with ethylene glycol (EG) and an anti-corrosion additive. The total height of the apparatus was approximately 2 m.

Thermal protection towards the side was provided by a concentric thermal shield N. In the original design, this shield was cooled or heated by a separate water circuit. In the rotating frame, we only had a single water circuit available, and it was needed for the top plate. Thus the shield N was temperature controlled at its mid-height by an electrical heater that was wound uniformly along its length. This arrangement precluded the operation of the system below the ambient laboratory temperature, which was near 22 °C. The temperature uniformity of the shield was not as good as it had been with the water cooling, and this contributed further, albeit only slightly, to a deterioration of the Nusselt-number accuracy. In a later version of the apparatus, the side shield was converted back to water or EG cooling/heating.

Most of the volume inside R that was not occupied by water or structural members was filled with low-density open-pore foam as shown in the photograph. The sample had two fill lines, one entering between the bottom plate anvil and the sidewall and the other entering similarly at the top plate. After complete filling of the sample, these fill lines were terminated in two small plastic containers, as shown in the photograph near the arrow from R. The pressure in these containers was referenced to the atmosphere by virtue of a small hole in the top of each.

2.2. *Thermometry and heaters*

The five thermometers in the bottom and the five in the top plate, as well as one thermometer on the bottom and one on the side shield, were calibrated in a separate calibration facility with a precision of a millikelvin against a Hart Scientific Model 5626 platinum resistance thermometer, which in turn had been calibrated against various fixed points on the ITS-90 temperature scale by the Hart Scientific Division of Fluke Corporation. Consistency between all of these thermometers is excellent; at the same temperature, their readings all agree within $\pm 0.002\,\mathrm{K}$.

The 20 sidewall thermometers (see § 2.5) were calibrated against the top- and bottom-plate thermometers after they had been installed in the sidewall. The plate temperatures were set so that $\Delta T = 0.1\,\mathrm{K}$ to ensure equilibration of the system in a reasonable time (half a day or so), and the sidewall thermometers were then assumed to be at the mean temperature T_m of the top and bottom plates.

The main bottom-plate heater was driven by an Agilent Model 6675 DC power supply. The current was taken to be given correctly by the power supply, and the voltage across the heater was measured for each data point with a second pair of leads. The bottom-shield and side-shield heaters were driven by Agilent Model E3634 DC power supplies using a two-lead method. All three heaters were operated in a digital feedback loop in conjunction with the relevant thermometer so as to hold the temperature in question constant.

2.3. *Typical experimental protocol*

Measurements using water as the convecting fluid and at several mean temperatures ranging from 23 ($Pr = 6.41$) to 60°C ($Pr = 3.05$) were made for a cylindrical sample with $\Gamma \simeq 1$. The sample had a height $L = 24.78 \pm 0.05$ and a diameter $D = 24.78 \pm 0.05\,\mathrm{cm}$, yielding an aspect ratio $\Gamma = D/L = 1.00$. The rotation rates were kept below $f = 0.3\,\mathrm{Hz}$, yielding Froude numbers $Fr \equiv \Omega^2(D/2)/g$ less than 0.05 for all runs and much smaller for most.

Readings of all thermometer resistances (see § 2.2) and of the bottom-plate heater current and heater-voltage were taken about every 3 s. The top (bottom) temperature T_t (T_b) was set equal to the average of the five thermometers embedded in the top (bottom) plate. For any given data point, measurements over typically the first 6 hours were discarded to avoid transients, and data taken over an additional period of at least another 6 hours were averaged to get the heat-current density Q, T_b and T_t. A near-negligible correction of T_t and T_b for the small temperature drops in the plates between the thermistors and the copper-fluid interfaces was made. No corrections were made for the finite conductance of the sidewall, as this had been shown to be negligible for the present conditions (Nikolaenko *et al.* 2005).

In nearly all cases, a sequence of measurements was carried out at constant ΔT, varying the angular speed Ω. Parameters for all runs are listed in table 1. Rayleigh numbers were determined from the temperature differences $\Delta T = T_b - T_t$, and from the fluid properties evaluated at $T_m = (T_t + T_b)/2$. For each T_m and ΔT (i.e. for each Pr and Ra) studied with rotation the Nusselt number was also determined without rotation, i.e. for $\Omega = 0$, and then the corresponding ratios $Nu(\Omega)/Nu(0)$ were computed. In order to eliminate the influence of the very small variations of Ra between different points in a given run at nominally constant Ra, we first computed $Nu(\Omega)/Ra^{0.3}$ and $Nu(0)/Ra^{0.3}$, which are nearly independent of Ra, and then used their ratio as the best estimate of $Nu(\Omega)/Nu(0)$.

In some cases, much longer runs were made in order to obtain better statistics on the properties of the LSC from the sidewall thermometers.

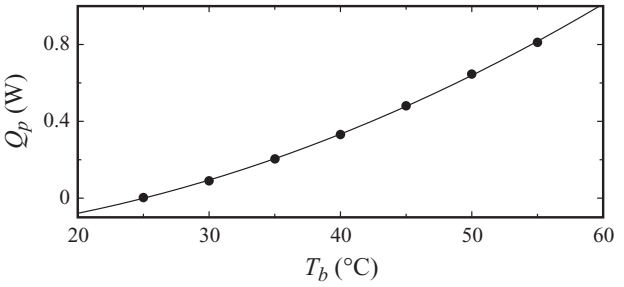

FIGURE 2. The parasitic heat current Q_p in Watts as a function of the bottom-plate temperature T_b in °C.

2.4. *Nusselt-number measurements*

Because of the imperfect temperature uniformity of the bottom shield (I in figure 1) discussed in § 2.1, there was a small parasitic heat loss Q_p from the bottom plate that depended on T_b. This had little influence on Nu at large Ra, where Q was large, but caused systematic errors at the smaller values of Ra. We determined $Q_p(T_b)$ by running the experiment with various T_m and with the very small $\Delta T = 0.1$ K. Using $\Delta T = 0.1$ K for this purpose was preferable because for $\Delta T = 0$ the thermal relaxation times of the system were too long to reach a stationary state in a reasonable time. With $\Delta T = 0.1$ K, nearly 10 h were required to reach a stationary state. Each run was conducted for one day and the data after about 16 h were used to evaluate Q, T_b and T_t. Under those conditions, we had $4 \times 10^7 \lesssim Ra \lesssim 9 \times 10^7$ depending on T_m, and expected $Nu/Ra^{0.304} \simeq 0.123$ ($Nu \simeq 24$). We adjusted Q_p until a corrected current $Q = Q_{appl} - Q_p$ (Q_{appl} is the Joule heating applied to the bottom plate) gave the expected results for Nu at this very small ΔT, where the result was very sensitive to Q_p. In figure 2, we show Q_p as a function of T_b. A quadratic polynomial fitted the data well, and was used to make the correction. We note that Q_p vanished just about at the ambient laboratory temperature, as it should. At other temperatures, it ranged up to about 0.8 W. Measurements of Nu used in the remainder of this paper were made with $1 \lesssim \Delta T \lesssim 32$ K, where $7 \lesssim Q \lesssim 600$ W; one sees that the correction for Q_p was small enough to be applied with confidence or even negligible.

A small correction to Nu was applied for the finite conductivity of the copper top and bottom plates. The size of this correction had been measured previously (Brown *et al.* 2005*b*); applying it increased Nu by 1.3 % at the largest $\Delta T = 32$°C ($Ra = 1.8 \times 10^{10}$), by 0.3 % at $\Delta T = 4$°C ($Ra = 2.2 \times 10^9$), and had little influence at lesser values of ΔT. It is unknown whether and how rotation may influence this correction.

2.5. *Sidewall-temperature measurements*

As discussed in previous publications (Brown *et al.* 2005*a*; Brown & Ahlers 2006*a*,*b*; Brown, Funfschilling & Ahlers 2007; Funfschilling *et al.* 2008), three sets of thermistors were inserted into blind holes in the sidewall so as to be within a millimetre or so of the fluid without penetrating into it. The three sets were at vertical positions $z = -L/4$, 0 and $L/4$ (we take the origin of the up-pointing vertical z-axis at the horizontal mid-plane of the sample). We shall refer to the levels as b for bottom at $z = -L/4$, m for middle at $z = 0$ and t for top at $z = L/4$. At each level, there were eight such thermistors equally spaced azimuthally. For the bottom set we were able to use only four of these because our total number of electrical feed-throughs out of the rotating frame was limited (after completion of the work discussed in the present paper this deficiency was remedied). The thermistors were able to sense the

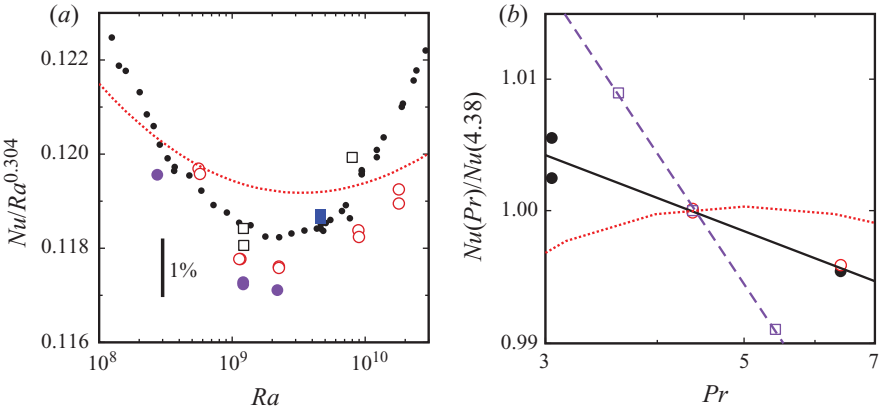

FIGURE 3. (Colour online) (*a*) The reduced Nusselt number $Nu/Ra^{0.304}$ for $\Omega = 0$ on a linear scale as a function of the Rayleigh number Ra on a logarithmic scale. Small solid circles (black online), strictly Boussinesq data from Funfschilling *et al.* (2005) for $Pr = 4.38$. Open squares (black online), $T_m = 60.00\,^{\circ}\mathrm{C}$ ($Pr = 3.05$). Solid squares (blue online), $T_m = 50.00\,^{\circ}\mathrm{C}$ ($Pr = 3.62$). Open circles (red online), $T_m = 40.00\,^{\circ}\mathrm{C}$ ($Pr = 4.38$). Solid circles (purple online), $T_m = 23.00\,^{\circ}\mathrm{C}$ ($Pr = 6.41$). Dotted line (red online), the model of Grossmann & Lohse (2001). (*b*) The ratio of $Nu(Pr)$ to $Nu(Pr = 4.38)$ as a function of the Prandtl number on logarithmic scales at several Rayleigh numbers. Solid circles (black online), $Ra = 1.2 \times 10^9$. Open circles (red online), $Ra = 2.2 \times 10^9$. Open squares (purple online), $\Gamma = 0.66$ and $3 \times 10^{10} \lesssim Ra \lesssim 2.0 \times 10^{11}$ from Nikolaenko *et al.* (2005). Solid line (black online), power-law fit to the solid circles which gave an exponent of -0.011. Dashed line (purple online), power-law fit to the open squares which gave an exponent of -0.044. Dotted line (red online), the model of Grossmann & Lohse (2001).

adjacent fluid temperature without interfering with delicate fluid-flow structures. We measured the temperature of each thermistor with a sampling period of about 3.5 s. Since the LSC carried warm (cold) fluid from the bottom (top) plate up (down) the sidewall, these thermistors detected the location of the upflow (downflow) of the LSC by indicating a relatively high (low) temperature.

To determine the orientation and strength of the LSC, we fit the function

$$T_f = T_{w,m} + \delta_m \cos\left(\frac{i\pi}{4} - \theta_m\right), \quad i = 0, \ldots, 7, \tag{2.1}$$

separately at each time step, to the eight temperature readings T_i obtained from the thermistors at height $z = 0$, least squares adjusting $T_{w,m}$, δ_m and θ_m. The fit parameter δ_m is a measure of the temperature amplitude of the LSC and θ_m is the azimuthal orientation of the plane of the LSC circulation. As defined here, the orientation θ_m is on the side of the sample, where the LSC is warm and up-flowing and is measured relative to the location of thermometer zero. We calculated mean temperature $T_{w,t}$, orientation θ_t, and amplitude δ_t for the top level at $z = L/4$ separately by the same method as for the middle row. For the bottom row (where only four equally spaced thermometers could be read), we calculated their average temperature $T_{w,b}$.

3. Results for the Nusselt number

All measurements of Nu (Ra, Pr, Ro) may be found in numerical form in a separate document submitted with this paper as supplementary material.

3.1. *Nusselt numbers for* $\Omega = 0$

In figure 3(*a*), we show the results for $\Omega = 0$ in the reduced form $Nu/Ra^{0.304}$ as a function of Ra on a logarithmic scale. Also shown are the 'strictly Boussinesq' data

from Funfschilling *et al.* (2005) for $Pr = 4.38$. One can see that most of the present data for $Pr = 4.38$ (open circles) fall about half a per cent below the reference data. This is within the possible systematic errors of the two data sets, due for instance to uncertainties in the sample heights and diameters (see Funfschilling *et al.* 2005). At the largest Ra there is a negative contribution from non-Boussinesq effects (Ahlers *et al.* 2006*a*), which at the largest Ra becomes as large as 0.7 %. No correction was made for this effect. Also shown, as a dotted line (red online), is the model of Grossmann & Lohse (2001) for $Pr = 4.38$. The overall agreement with the data is quite good, although the Ra-dependence seems slightly different.

Note that the apparent 'scatter' of the points, most noticeable near $Ra = 1 \times 10^9$, is actually not scatter at all, but rather reveals a small dependence of Nu on Pr. In order to illustrate this in more detail, we show some of the data from figure 3(*a*) in figure 3(*b*) as a function of Pr. There we divided the results by the experimental measurements at $Pr = 4.38$. One sees that, for $Ra = 1.2 \times 10^9$ (solid circles) and for $Ra = 2.2 \times 10^9$ (open circles), Nu decreased very slightly as Pr increased. This can be described by an effective power-law-dependence $Nu \propto Pr^{\alpha}$ with $\alpha \simeq -0.01$, as shown by the solid line in the figure. This is a weaker dependence on Pr than was reported earlier (Nikolaenko *et al.* 2005), and shown by the open squares and the dashed line, for a sample with $\Gamma = 0.66$ and $Ra \simeq 10^{11}$. It is, however, quite consistent with earlier measurements for $\Gamma = 1.00$ (Ahlers & Xu 2001; Xia, Lam & Zhou 2002) over a much wider range of Pr. The new data are also consistent with those of Roche *et al.* (2002), which according to those authors imply at most a very mild dependence of Nu on Pr, corresponding to $|\alpha| \leqslant 0.03$. Our new data imply that the expected maximum in $Nu(Pr)$ (Grossmann & Lohse 2001) occurs at or below $Pr = 3$, whereas the GL model gives a maximum near $Pr = 5$ as shown by the dotted line (red online) in figure 3(*b*). Most likely the small differences between the model and the data could be eliminated by an adjustment of the model parameters.

We expect that any small systematic errors in Nu will be essentially the same with and without rotation, and thus that the ratio $Nu(\Omega > 0)/Nu(\Omega = 0)$ will not be influenced by them. The precision of the data for Nu depends somewhat on the size of ΔT and on the duration of the run over which measurements are averaged. For $\Delta T \gtrsim 4\,\mathrm{K}$ it is believed to be near 0.1 %. For smaller ΔT somewhat larger systematic errors, independent of Ω, are possible because of systematic uncertainties in the temperature scales of the top- and bottom-plate thermometers. However, these errors should not affect the ratio $Nu(\Omega)/Nu(0)$. For the smallest $\Delta T \simeq 1\,\mathrm{K}$ random errors due to temperature resolution are expected to be a few tenths of 1 %.

3.2. *Nusselt numbers for* $\Omega > 0$

3.2.1. *Qualitative features*

Two representative sets of data for $Nu(\Omega)/Nu(0)$ as a function of $1/Ro$ on a logarithmic scale are shown in figure 4. One sees that there are several distinct ranges, with different characteristic variations of $Nu(\Omega)$ with Ω or $1/Ro$. To the left of the short vertical dotted line there was very little change of Nu with $1/Ro$, although as we shall see in § 3.2.2, Nu was not strictly constant. At the location of the vertical dotted line, which we shall call $1/Ro_c$, there was a sharp transition, or bifurcation, to a different state where Nu initially increased dramatically and then decreased strongly with increasing $1/Ro$. At the bifurcation, $Nu(\Omega)$ was continuous; thus the bifurcation was supercritical. This phenomenon has been reported before by Stevens *et al.* (2009), and upon close inspection it can already be seen in the DNS of Kunnen, Clercx & Geurts (2008*b*). As $1/Ro$ increased beyond $1/Ro_c$, Nu first increased linearly with

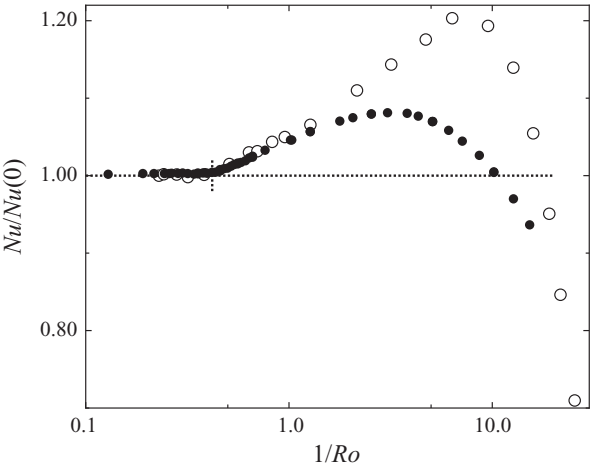

FIGURE 4. The ratio $Nu(\Omega)/Nu(\Omega=0)$ as functions of $1/Ro$ on a logarithmic scale. Solid circles, run E6, $Ra=2.25\times10^9$ and $Pr=4.38$. Open circles, run E2, $Ra=2.73\times10^8$ and $Pr=6.26$. The short vertical dotted line corresponds to the approximate location of the bifurcation point at $1/Ro_c$.

$1/Ro$. Qualitatively, the strong increase at modest rotation rates has been observed by several investigators, including Rossby (1969), Zhong *et al.* (1993), Liu & Ecke (1997*b*), Liu & Ecke (2009), King *et al.* (2009). It is understood to be caused by the Ekman vortices (Hart 1995, 2000; Julien *et al.* 1996*b*; Hart *et al.* 2002; Kunnen *et al.* 2006; Zhong *et al.* 2009; Stevens *et al.* 2010*b*) that form in the presence of the Coriolis force; these vortices extract additional warm (cold) fluid from the bottom (top) thermal BL. Since the enhancement of Nu started discontinuously at $1/Ro_c$, we are led to conclude that the Ekman vortices formed only above this threshold. With further increase of $1/Ro$ one sees a dramatic decrease of Nu. In this range, the depression of Nu due to the TP effect was stronger than the Ekman enhancement, and Nu reached values well below those without rotation. Of course, it is known that sufficiently large rotation rates will suppress the convective heat transport completely, leading to $Nu=1$ when the rotation has increased the critical Rayleigh number $Ra_c(\Omega)$ (Chandrasekhar 1981) up to the value of Ra for the particular run. The transition from the turbulent-convection regime to the regime near the onset of convection was considered in some detail recently by King *et al.* (2009).

3.2.2. *The range* $1/Ro<1/Ro_c$

In figure 5, we show data for $1/Ro\leqslant0.7$ for all runs that resolved this range. The labels in each panel give, from left to right, the run number, $Ra/10^9$, and Pr (see also table 1). The bifurcation at $1/Ro_c$ is apparent for several of the runs. However, especially from the data at relatively small Pr and large Ra, one sees that the rotation already has an influence on Nu in the range below $1/Ro_c$. Runs E7, E8 and E9 clearly show that there is an initial small enhancement, followed by a small depression, of Nu. For all cases studied in this work, these effects are less than 1 %. The results for the time-averaged and azimuthally averaged thermal gradient, and of the thermal amplitude of the LSC, to be presented in §§4 and 5.2, respectively, likewise indicate that interesting modifications of the system occur already in this range below $1/Ro_c$. To our knowledge the origin of these phenomena is not clear at this time, although one might expect that in part they could be explained by considerations involving

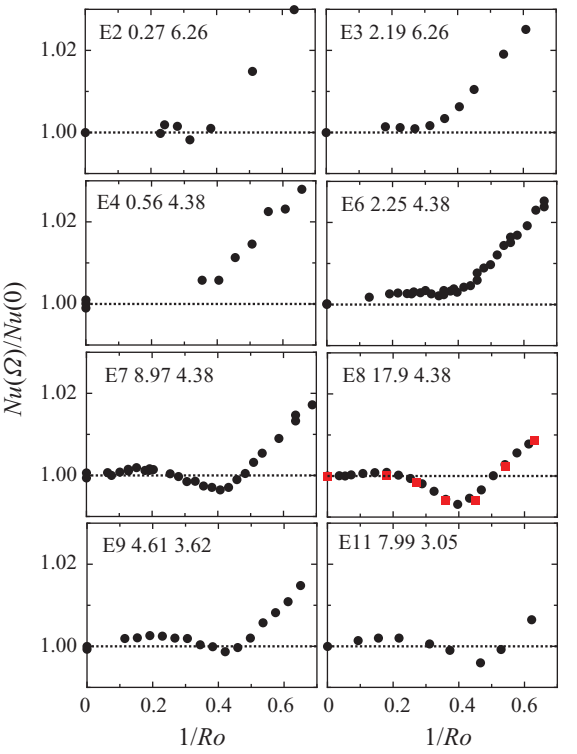

FIGURE 5. (Colour online) The ratio $Nu(\Omega)/Nu(\Omega=0)$ as functions of $1/Ro$ at small $1/Ro$. The labels in each panel give, from left to right, the run number, $Ra/10^9$, and Pr (see also table 1). For the case E8 the solid circles and solid squares (red online) represent data taken during different time periods separated by about six months and show the long-term reproducibility of some of the observed phenomena.

centripetal forces and differential rotation at different heights in the sample such as those pursued recently by Stevens *et al.* (2010*a*). It seems unlikely that TP suppression of Nu would play any role in this range of $1/Ro$.

3.2.3. *The dependence of* $1/Ro_c$ *on Ra and Pr*

In our work, the bifurcation at $1/Ro_c$ always occurred at relatively small rotation rates, and for that reason, was difficult to determine with high accuracy. Nonetheless, we were able to obtain the data shown in figure 6 as a function of Ra (figure 6*a*) and of Pr (figure 6*b*). We obtained $1/Ro_c$ from the intercept of two straight lines. For the runs where adequate measurements existed, one line was placed through the data just below and the other through the data just above the transition. The results do not resolve any significant dependence on Ra, but do show a significant dependence on Pr. The Pr-dependence can be represented by an effective power law $1/Ro_c = a\,Pr^{\zeta}$, with $a = 0.77 \pm 0.05$ and $\zeta = -0.42 \pm 0.04$, which is shown as the solid line in the figure. We do not necessarily expect this relation to be valid much beyond the quite narrow Pr range of our data. Thus, for instance, it is known from DNS (Zhong *et al.* 2009; Stevens *et al.* 2010*a*) that there is no enhancement of Nu, and most likely no bifurcation, for $Pr \lesssim 1$ and Ra near 10^8 or less. It was also shown by experiment on a sample with $\Gamma = 0.50$ (Niemela *et al.* 2010) at the very large $Ra \simeq 4 \times 10^{15}$ and Pr near six that Nu decreases with increasing $1/Ro$ as soon as

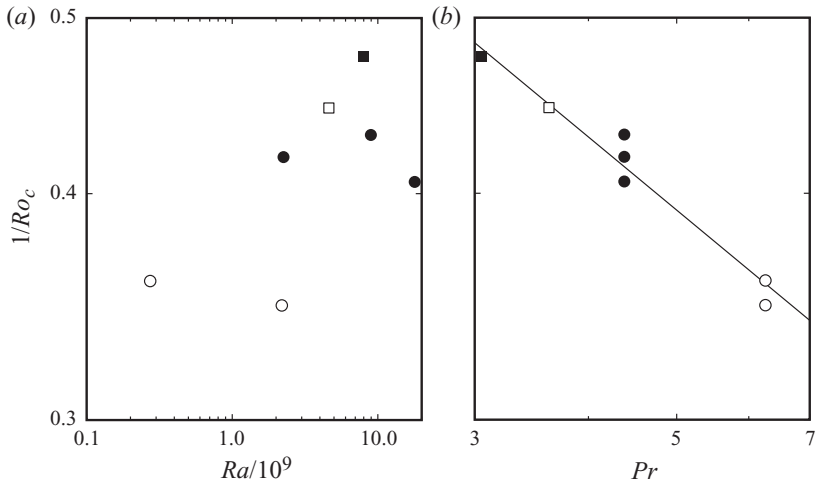

FIGURE 6. The critical inverse Rossby number $1/Ro_c$ as a function of the Rayleigh number (a) and of the Prandtl number (b) on logarithmic scales. Open circles, $Pr = 6.26$; solid circles, $Pr = 4.38$; open squares, $Pr = 3.62$; solid squares, $Pr = 3.05$. The solid line is a power law with an exponent $\zeta = -0.42$.

rotation starts, implying that there is no bifurcation at a finite $1/Ro_c$. Understanding the origin of the Pr-dependence, and indeed of the very existence, of the bifurcation point in our parameter range remains an interesting challenge.

3.2.4. *The dependence of the initial slope S_1 of $Nu(\Omega)/Nu(0)$ on Ra and Pr*

One can see from the data in figure 5 and just above $1/Ro_c$ that Nu increased linearly beyond the bifurcation point. This increase was attributed (Zhong *et al.* 2009) to Ekman pumping. However, for $1/Ro > 1/Ro_c$ we expect two competing effects. Ekman pumping will enhance and the TP effect will diminish the heat transport. Without theoretical guidance it is not possible to rigorously separate these two phenomena in a quantitative analysis of the data. Consistent with the data, we shall assume that the Ekman pumping is responsible for the linear rise of Nu above the bifurcation, and that the TP suppression is of quadratic or higher order so that it comes into play only as $1/Ro$ becomes larger. Of course, we cannot rule out that the linear rise is the net result of a positive contribution from Ekman pumping and a smaller but negative contribution from the TP effect.

We fit the available data above but close to $1/Ro_c$ to a straight line. This yielded the initial slope S_1 of $Nu(\Omega)/Nu(0) = S_0 + S_1 \cdot (1/Ro) + \cdots$. The results for S_1 are shown in figure 7 as a function of Ra (figure 7a) and of Pr (figure 7b). As was the case for $1/Ro_c$, the measurements of S_1 do not reveal any dependence on Ra, except that the point at the largest Ra (run E8, $\Delta T = 31.7$ K, see table 1) falls well below the other three at the same Pr. Because of the exceptionally large value of ΔT for this point, we expect that the low value may be attributable to non-Boussinesq effects (Ahlers *et al.* 2006*a*). However, the recent work by Niemela *et al.* (2010) for the very large $Ra = 4.3 \times 10^{15}$, $\Gamma = 0.50$ and $Pr = 5.9$ showed that $Nu(\Omega) \propto (1/Ro)^{-0.024}$, corresponding to a depression of Nu due to rotation. It is possible that our low value of S_1 for our largest Ra is due to this observed decrease of the heat transport by the Ekman-pumping effect with increasing Ra. Thus, it would be interesting to obtain strictly Boussinesq data over the Ra range from 10^{11} to 10^{15}.

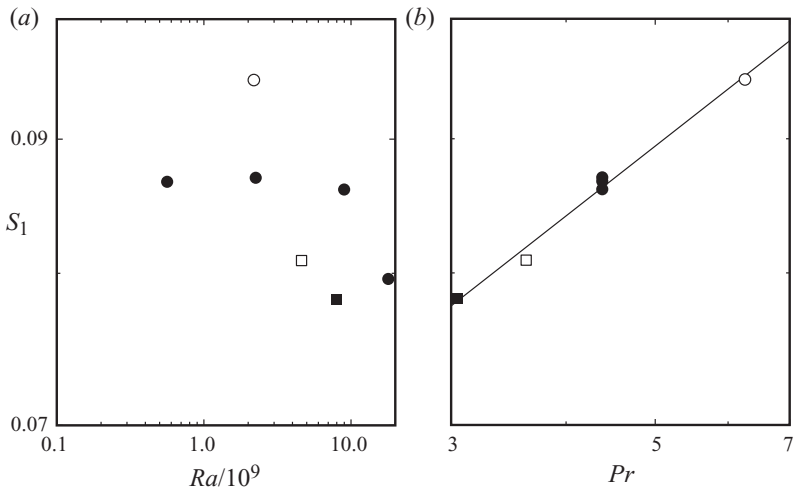

FIGURE 7. (*a*) The initial slope S_1 of $Nu(\Omega)/Nu(0) = b + S_1 \cdot (1/Ro) + \cdots$ as a function of Ra. (*b*) The initial slope S_1 as a function of Pr. The scales of both axes are logarithmic. Open circles, $Pr = 6.26$; solid circles, $Pr = 4.38$; open squares, $Pr = 3.62$; solid squares, $Pr = 3.05$. The solid line is a power law with an exponent $\eta = 0.27$.

It is already apparent from figure 4 that S_1 does not depend strongly on Pr. However, as was the case for $1/Ro_c$, at a quantitative level there is a modest increase of S_1 with Pr (see figure 7*b*) over our parameter range. The solid line corresponds to $S_1 = S_{1,0} Pr^{\eta}$ with $S_{1,0} = 0.058 \pm 0.002$ and $\eta = 0.27 \pm 0.02$. Although this power law may provide a useful representation of the data, we again do not expect it to hold necessarily much beyond the data range. We note again that, at least for $Ra = O(10^8)$, DNS has indicated (Zhong *et al.* 2009) that there is no positive enhancement of Nu for $Pr \lesssim 1$; thus our empirical fit, which yields a positive slope $S_1 = 0.058$ for $Pr = 1$, ceases to be meaningful in that range. We note that the heat transport by Ekman pumping (which we assumed to be exclusively responsible for a positive slope S_1) increases as Pr increases, as previously reported. However, the effect is modest; S_1 increased by less than 20 % as Pr changed by about a factor of two. Again, as seen in figure 4 and as will be discussed in the next section, the main change with decreasing Pr and increasing Ra is an enhancement of the suppression of Nu below the initial increase attributed to Ekman pumping. We attribute this suppression to the TP effect and see that it leads to a strong Pr-dependence at intermediate to large $1/Ro$.

3.2.5. *The range of* $1/Ro$ *well above the bifurcation*

As seen already in figure 4, Nu initially increases due to the Ekman pumping, but then decreases again due to the TP effect. In figure 8, we show more data for other Pr and Ra values. Figure 8(*a*) gives the results for the three values $Pr = 3.05$, 4.38 and 6.42 at the same $Ra = 1.2 \times 10^9$. At (not too small) constant $1/Ro$ one sees a dramatic increase of $Nu(\Omega)/Nu(0)$ with increasing Pr. Some of this increase comes from an increase in the efficiency of the heat transport by the Ekman-pumping effect. However, we see from figure 7 that the increase in S_1 over this range of Pr is less than 20 %, while the effect of Pr on Nu seen in figure 8(*a*) is much larger. We conclude that the depression of Nu due to the TP effect depends strongly on Pr and is larger at smaller Pr.

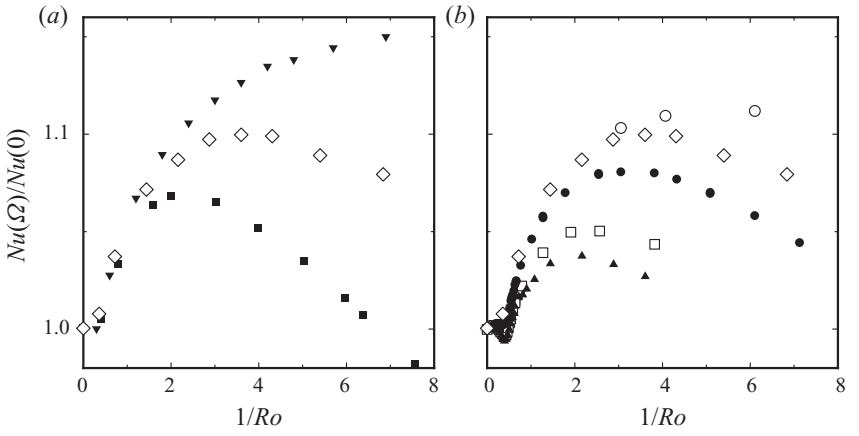

FIGURE 8. The ratio $Nu(\Omega)/Nu(\Omega=0)$ as functions of $1/Ro$. (*a*) Results for $Ra \simeq 1.2\times10^9$ at several Prandtl numbers. Solid squares, run E11 ($Pr=3.05$). Open diamonds, Run E5 ($Pr=4.38$). Solid downward triangles, run E1 ($Pr=6.42$). (*b*) Results for $Pr=4.38$ at several Rayleigh numbers. Solid up-pointing triangles, run E8 ($Ra=1.8\times10^{10}$). Open squares, run E7 ($Ra=8.9\times10^9$). Solid circles, run E6 ($Ra=2.2\times10^9$). Open diamonds, run E5 ($Ra=1.2\times10^9$). Open circles, run E4 ($Ra=5.6\times10^8$).

Let us consider the decrease of $Nu(\Omega)/Nu(0)$ with decreasing Pr along a vertical line in figure 8(*a*), i.e. along a line of constant (not too small) $1/Ro$ and at constant Ra. We note that along that line the inverse Ekman number $1/Ek$ increases when Pr decreases (see also table 1), indicating that the Coriolis force (which generates the TP effect) increases relative to the viscous force. Thus, as seen in the experiment, one would expect the TP effect (which is inhibited by viscous dissipation) to become stronger as Pr decreases; but of course we do not have a quantitative theory.

Figure 8(*b*) shows results for $Nu(\Omega)/Nu(0)$ for several values of Ra at constant $Pr=4.38$. In § 3.2.4, we saw that the Ekman-pumping enhancement of Nu just above $1/Ro_c$ was independent of Ra within our resolution. However, the data suggest that the TP depression depends strongly on Ra, and increases as Ra increases. For Ra near 4×10^{15} we learned from the measurements of Niemela *et al.* (2010) for $\Gamma=0.5$ that this depression eventually will become strong enough to completely eliminate any enhancement, leading to a depression of Nu that starts as soon as $1/Ro$ exceeds zero.

3.3. *The Nusselt number as a function of the Taylor number*

It is useful to see the relationship of our measurements to some other results in the literature. In figure 9(*a*), we show the location of our data points for $Pr=4.38$ in the Ta–Ra parameter space (the data at other Pr cover similar ranges). Our measurements were made at constant applied temperature difference, varying the rotation rate Ω, i.e. at constant Ra as a function of Ta or Ek and of Ro. Thus they fall along horizontal lines in the figure. For our data, the locus $Ro=1$ is shown by the dotted line. Often measurements by others were made at constant Ω (i.e. constant Ta or Ek), varying the applied temperature difference (i.e. Ra and Ro). Those data then would fall along vertical lines in figure 9(*a*). The results of Liu & Ecke (2009) fall approximately into the rectangle in the lower left of the figure. Those of King *et al.* (2009) are in the range below the dashed line. The heavier solid line in the

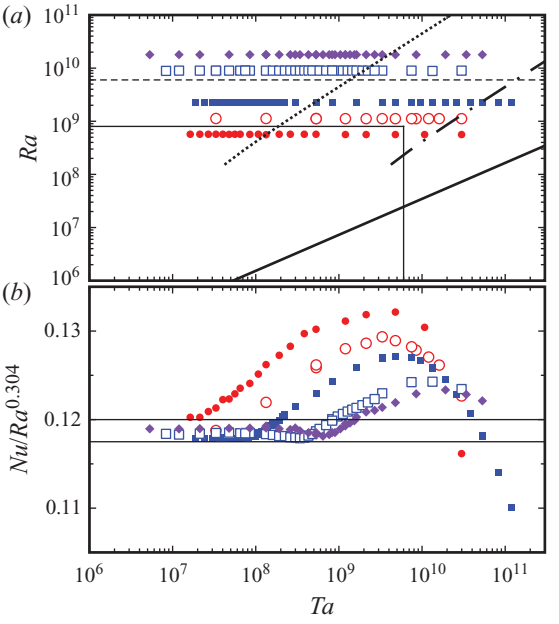

FIGURE 9. (Colour online) (*a*) Location of the measurements for $Pr = 4.38$ in the Ra–Ta parameter space. The dotted (dash-dotted) line corresponds to $1/Ro = 1$ ($1/Ro = 10$) for our data. The rectangle in the lower left indicates the approximate range covered by the data of Liu & Ecke (2009). The data of King *et al.* (2009) are for parameters in the range below the dashed line. The thicker solid line is the location of the critical Rayleigh number for the onset of convection. Solid circles (red online): run E4. Open circles (red online), run E5. Solid squares (blue online), run E6. Open squares (blue online), run E7. Solid diamonds (purple online), run E8. (*b*) The reduced Nusselt number $Nu/Ra^{0.304}$ as a function of the Taylor number. The symbols are as in (*a*). Results without rotation ($Ta = 0$) depend slightly on Ra (see figure 3) but fall between the two horizontal lines.

figure is the location of the onset of convection at $Ra = Ra_c(Ta)$ (Chandrasekhar 1981).

In figure 9(*b*), we show our results for the reduced Nusselt number $Nu/Ra^{0.304}$ as a function of Ta for the Ra values explored for $Pr = 4.38$. The two thin horizontal lines indicate the range covered by $Nu/Ra^{0.304}$ in the absence of rotation (see figure 3). The discontinuous onset of the Nusselt enhancement due to Ekman pumping can also be seen in this representation. However, the critical value Ta_c for that onset depends strongly upon Ra, whereas $1/Ro_c$ at constant Pr had been found to be independent of Ra (see figure 6). Below that onset the rotation had only a minor influence on the heat transport, as seen from the fact that the data fall more or less between the two horizontal lines. As Ta increases, the Ekman enhancement is followed by the TP suppression, with the suppression generally being stronger as the data points approach the bifurcation line $Ra_c(Ta)$ more closely. The bifurcation line can be regarded as the locus of complete TP domination, where the Nusselt number is suppressed all the way to $Nu = 1$. In the range of very strong TP suppression, only somewhat above the convective onset, some have suggested that $Nu \sim Ra^{6/5}$ (King *et al.* 2009); but the range over which such a power law represents the data is quite narrow and thus it seems questionable to us whether it is useful to describe $Nu(Ra)$ in this way. In any case, any extrapolation of such a power law beyond the range of the data from which it was derived is unjustified.

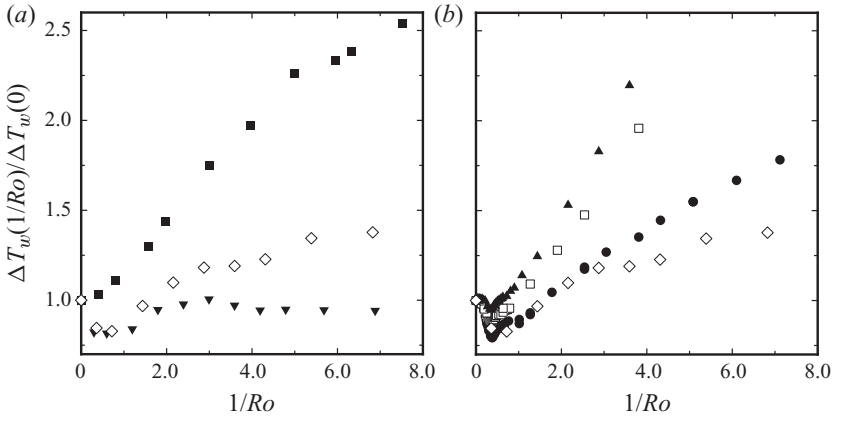

FIGURE 10. Normalized vertical temperature variation $\Delta T_w(1/Ro)/\Delta T_w(0)$ along the sidewall. (*a*) Results for $Ra = 1.2 \times 10^9$. Solid squares: $Pr = 3.05$ (E10, $T_m = 60.0\,^\circ$C, $\Delta T = 1.21$ K). Open diamonds: $Pr = 4.38$ (E5, $T_m = 40.0\,^\circ$C, $\Delta T = 1.99$ K). Solid downward-pointing triangles: $Pr = 6.42$ (E1, $T_m = 23.0\,^\circ$C, $\Delta T = 4.68$ K). (*b*) Results for $Pr = 4.38$ ($T_m = 40.00\,^\circ$C). Solid upward-pointing triangles: $Ra = 1.8 \times 10^{10}$ (E8, $\Delta T = 31.69$ K). Open squares: $Ra = 8.9 \times 10^9$ (E7, $\Delta T = 15.87$ K). Solid circles: $Ra = 2.2 \times 10^9$ (E6, $\Delta T = 3.98$ K). Open diamonds: $Ra = 1.2 \times 10^9$ (E5, $\Delta T = 1.99$ K).

4. Temperature gradients near the sidewall

Without rotation and away from the thermal BLs the time-averaged temperature in a cylindrical RBC system is known to be nearly uniform along the vertical centreline. Depending on Pr, the small prevailing temperature gradient can be either stabilizing or destabilizing (Tilgner, Belmonte & Libchaber 1993; Brown & Ahlers 2007*b*). The situation is different near the sidewall. Plumes emitted by the top and bottom thermal BLs tend to be swept by the LSC and to travel upwards mostly near the wall. This leads to a significant destabilizing vertical gradient which, depending on Ra and Pr, can be 10 % or more of $\Delta T/L$ (Brown & Ahlers 2007*b*). DNS showed that rotation leads to a much larger destabilizing temperature gradient along the centreline (Julien *et al.* 1996*b*; Hart & Olsen 1999; Kunnen *et al.* 2010). This effect was attributed to diminished vertical and enhanced lateral mixing in the presence of rotation (Julien *et al.* 1996*b*). Here we report on the effect of rotation on the temperature gradient near the wall.

The fits of (2.1) to the three sets of sidewall temperatures gave the azimuthally averaged mean temperatures $T_{w,m}$, $T_{w,t}$ and $T_{w,b}$ along the wall at the three vertical positions $L = 0$, $L/4$ and $-L/4$, respectively. These in turn yielded the vertical temperature variation along the wall and away from the top and bottom BLs.

For $\Omega = 0$ the estimate $\Delta T_w/\Delta T \equiv 2 \times \langle T_{w,b} - T_{w,t} \rangle_t / \Delta T$ of the time-averaged vertical temperature variation along the entire sample (excluding the BLs) was reported by Brown & Ahlers (2007*b*) for a sample of the same size and shape as the one used in the present work. Here we show $\Delta T_w(1/Ro)/\Delta T_w(0)$ in figure 10 (results for $\Delta T_w/\Delta T$ for run E7 were reported by Stevens *et al.* 2009). In figure 10(*a*), results at constant $Ra = 1.2 \times 10^9$ are shown for three values of Pr. At small $Pr \simeq 3$ and over a wide range of $1/Ro$ one sees a dramatic enhancement of the temperature variation. As Pr increases, this effect becomes smaller. Figure 10(*b*) shows the results at constant Pr as a function of Ra. Again, the enhancement is evident, with a larger effect observed at the larger Ra values.

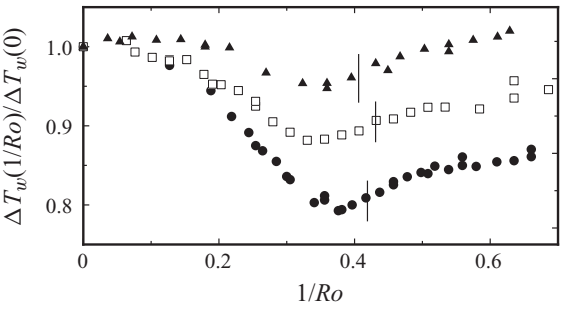

FIGURE 11. Normalized vertical temperature variation $\Delta T_w(1/Ro)/\Delta T_w(0)$ along the sidewall for small $1/Ro$ and for $\mathrm{Pr} = 4.38$ ($T_m = 40.00\,^{\circ}\mathrm{C}$). Solid upward-pointing triangles: $Ra = 1.8 \times 10^{10}$ (E8, $\Delta T = 31.69\,\mathrm{K}$). Open squares: $Ra = 8.9 \times 10^{9}$ (E7, $\Delta T = 15.87\,\mathrm{K}$). Solid circles: $Ra = 2.2 \times 10^{9}$ (E6, $\Delta T = 3.98\,\mathrm{K}$). The data for run E7 were reported by Stevens *et al.* (2009). The short vertical lines give the location of $1/Ro_c$ determined from the Nusselt-number measurements.

At small $1/Ro$ there is interesting structure in this variable, as shown in figure 11 for $Pr = 4.38$ and several Ra. One sees that there is an initial decrease in the temperature gradient with increasing rotation rate, followed by an increase above a characteristic value of $1/Ro$. It is interesting to note that the relatively sudden change from a decreasing to an increasing gradient occurs at a value of $1/Ro$ that is below rather than at the $1/Ro_c$ determined from the Nusselt-number measurements and shown by the short vertical lines in the figure.

The overall increase, over a wide range of $1/Ro$, of ΔT_w can be attributed qualitatively to enhanced plume detachment from the BLs, which leads to a greater plume density near the sidewall, as well as to enhanced Ekman-vortex activity. This phenomenon is evident in the recent DNS of Zhong *et al.* (2009). The initial decrease of ΔT_w at small rotation rates is accompanied by an enhanced strength of the LSC, as we shall see below in § 5.2.

5. The large-scale circulation

5.1. *Reynolds numbers of the large-scale circulation*

For cylindrical samples with $\Gamma \simeq 1$ and $\Omega = 0$ there have been numerous measurements of the frequencies or periods of characteristic oscillatory modes of the system by several methods. Single-point temperature and velocity determinations have been used, and auto-correlation functions as well as cross-correlation functions of temperature time series at various locations in the sample have been determined. In most if not all of these measurements, it is now understood that the detected oscillations are caused by a torsional (Funfschilling & Ahlers 2004; Funfschilling *et al.* 2008) or sloshing (Brown & Ahlers 2009; Xi *et al.* 2009; Zhou *et al.* 2009) mode of the LSC dynamics with a frequency that is synchronous with the LSC turnover frequency, provided Ra is not too large (Brown *et al.* 2007); at most locations in the sample the torsional mode leads to synchronous temperature and velocity oscillations. This was discussed recently in some detail by Brown *et al.* (2007) (see also Xia 2007), who also give extensive references to the literature. Here we cite only the particularly noteworthy work of Qiu & Tong (2002), who showed that velocity- and temperature-oscillation measurements on the same sample do indeed

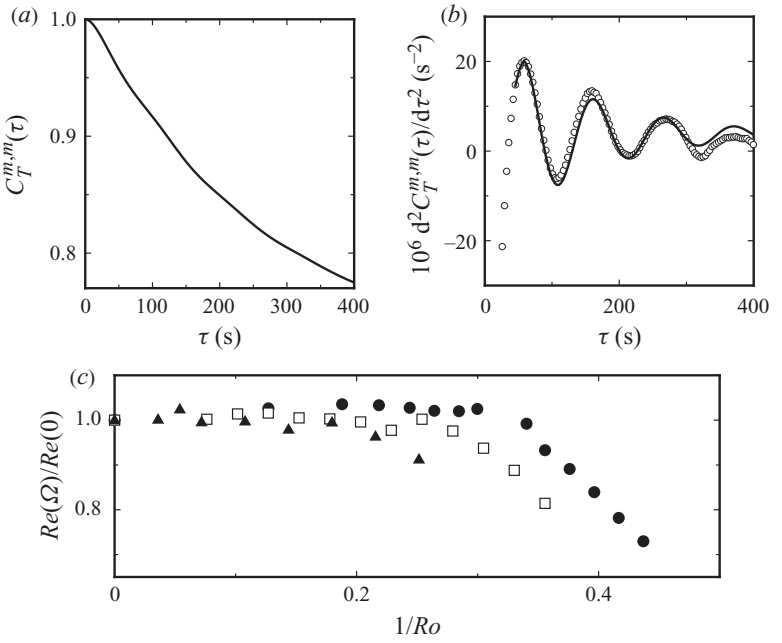

FIGURE 12. (*a*) Average $C_T^{m,m}(\tau)$ of the auto-correlation functions of the eight sidewall temperatures at the horizontal mid-plane for run E6 ($Ra = 2.2 \times 10^9$, $Pr = 4.38$) and $\Omega = 0$ Hz. (*b*) The second derivative of $C_T^{m,m}(\tau)$ in (*a*). Open circles, experimental data. Solid curve, fit of the function $C_{fit} = c_1 \exp(-\tau/\tau^{bg}) \cos(2\pi * \tau/\tau^{ac})$ to the data which gave $\tau^{ac} = 104.7$ s. (*c*) The normalized Reynolds numbers $Re(\Omega)/Re(0)$ as function of $1/Ro$ at $Pr = 4.38$. Solid circles, $Ra = 2.25 \times 10^9$ (run E6). Open squares, $Ra = 8.97 \times 10^9$ (run E7). Solid triangles, $Ra = 1.79 \times 10^{10}$ (run E8).

yield the same frequencies. The large body of previous work shows that any one of the above-mentioned measurements can be used to compute a Reynolds number Re of the LSC, provided Ra is less than some characteristic $Ra^* \simeq 3 \times 10^9$. Even for $Ra > Ra^*$, differences between Re determined by different methods are not very large. Since we are concerned here with the $1/Ro$-dependence of Re, we shall focus on $Re(\Omega)/Re(0)$, which we assume to be insensitive to the measurement that was done even for $Ra > Ra^*$.

In the present paper, we determined Re from auto-correlation functions of the eight sidewall temperatures $T_{m,i}$ at the middle ($z = 0$) location

$$\tilde{C}_{T_i}^{m,m}(\tau) = \langle [T_{m,i}(t) - \langle T_{m,i} \rangle_t] \times [T_{m,i}(t+\tau) - \langle T_{m,i} \rangle_t] \rangle_t, \tag{5.1}$$

separately at each azimuthal location i. We normalized these correlation functions to form

$$C_{T_i}^{m,m}(\tau) = \tilde{C}_{T_i}^{m,m}(\tau)/\tilde{C}_{T_i}^{m,m}(0). \tag{5.2}$$

Finally, we computed the average $C_T^{m,m}(\tau)$ of $C_{T_i}^{m,m}(\tau)$ over all eight azimuthal locations $i = 0, \ldots, 7$.

Figure 12(*a*) shows the averaged auto-correlation function $C_T^{m,m}(\tau)$. The overall decay is obvious; but close inspection also reveals an oscillatory component. To make the oscillations more dominant, we took the second derivative with respect to τ, which yielded the result shown in figure 12(*b*). This result could be fitted fairly well

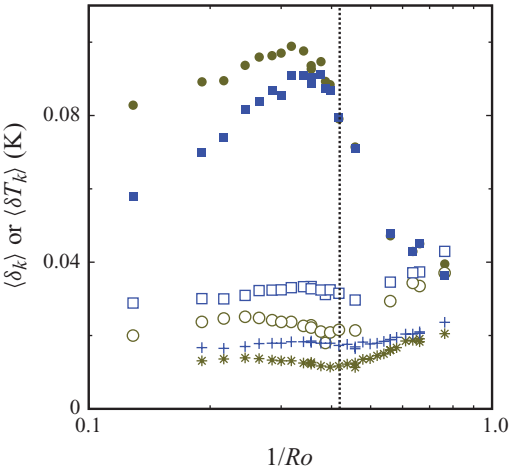

FIGURE 13. (Colour online) Some properties of the LSC for $Ra = 2.25 \times 10^9$, $Pr = 4.38$ (run E6, $\Delta T = 3.98$ K) as a function of $1/Ro$ on a logarithmic scale. Solid symbols: the time-averaged LSC amplitudes $\langle\delta_k\rangle$ for $k = m$ (circles, green) and $k = t$ (squares, blue). Open symbols: the root-mean-square deviations $\langle\delta T_k\rangle$ from the fits of (2.1) for $k = m$ (circles, green) and $k = t$ (squares, blue). Stars and pluses: the time averages of the probable errors of δ_k for $k = m$ (stars, green) and $k = t$ (pluses, blue). The vertical dotted line corresponds to $1/Ro_c$ as determined from the Nusselt-number measurements.

by the function

$$C_{fit} = c_1 \exp(-\tau/\tau^{bg}) \cos(2\pi * \tau/\tau^{ac}). \tag{5.3}$$

This fit yielded $\tau^{ac} = 104.7 \pm 0.7$ for this particular case. We took the ratio $\tau^{ac}(\Omega)/\tau^{ac}(0)$ to be equal to $Re(\Omega)/Re(0)$. Results for this ratio are shown in figure 12(*c*) for $Pr = 4.38$ and three different values of Ra. Quite remarkably, slow rotation, up to $1/Ro \simeq 0.3$ or so, had little or no effect upon Re. This differs from the $1/Ro$-dependence of the temperature gradient near the sidewall (see § 4 and figure 11), which decreased at much smaller $1/Ro$, and the LSC temperature amplitude $\langle\delta_k\rangle$ (see § 5.2 and figure 13) which increased as soon as rotation was started. However, for $1/Ro \gtrsim 0.3$ Re did decrease. This decrease started well below $1/Ro_c \simeq 0.41$ as determined from the Nusselt-number measurements (see § 3.2.3 and figure 6). The decrease of $Re(\Omega)/Re(0)$ seemed to start at a smaller value of $1/Ro$ for the larger Ra. We were unable to measure $Re(1/Ro)$ for larger $1/Ro$ because we did not observe well-defined oscillations in the correlation functions. However, an explanation of the various $1/Ro$-dependences at small $1/Ro$ will already be an interesting challenge.

5.2. *Strength of the large-scale circulation in the presence of rotation*

It is generally believed that the formation of the Ekman-vortex structures diminishes the strength of the LSC, and that for $1/Ro$ significantly above unity, the LSC ceases to exist (see e.g. Hart *et al.* 2002 and Kunnen *et al.* 2008*b*). Here we report on the $1/Ro$-dependences of the temperature amplitudes δ_k, $k = m, t$ of the LSC that were obtained by fitting (2.1) to the sidewall-temperature measurements at the two vertical levels $z = 0$ ($k = m$) and $z = L/4$ ($k = t$) as described in § 2.5. We find that the $\langle\delta_k\rangle$ initially increase, and then decrease, with increasing $1/Ro$. Near $1/Ro \simeq 1$ they become comparable to the root-mean-square temperature fluctuations about the

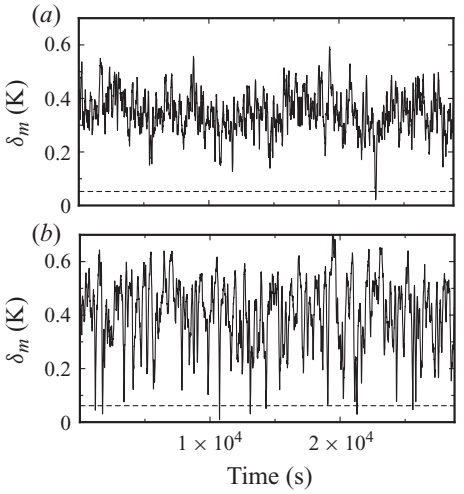

FIGURE 14. Time series of the temperature amplitude δ_m for $1/Ro = 0$ (a) and for $1/Ro = 0.26$ (b). The data are for run E8, $Ra = 1.8 \times 10^{10}$ and $Pr = 4.38$. The dashed line shows the threshold value $\delta_l = 0.15 * \langle \delta_m \rangle$ used to define cessations (see text).

fit and a more detailed analysis would be required to determine whether the LSC continues to exist in the presence of these large fluctuations.

In figure 13, we show the time-averaged LSC temperature amplitudes $\langle \delta_k \rangle$, $k = m, t$, as solid symbols as a function of $1/Ro$ on a logarithmic scale. Similar data, for run E7, were shown by Stevens *et al.* (2009). The dotted vertical line corresponds to $1/Ro_c$ as determined from the Nusselt-number measurements. At very small $1/Ro$, the amplitudes at $z = 0$ and $z = L/4$ differ somewhat from each other as had been noted before (Brown & Ahlers 2007*b*); but with increasing rotation rate both increase and approach each other. The amplitudes merge near a maximum that is located somewhat below $1/Ro_c$ and then decrease with increasing $1/Ro$. The origin of the initial increase of the $\langle \delta_k \rangle$ is not obvious, but may be associated with the centripetal effects discussed by Stevens, Clercx & Lohse (2010*a*). Similarly, it is unclear why the maximum of $\langle \delta_k \rangle$ should be located well below $1/Ro_c$. With increasing rotation rate beyond the one of the maximum the amplitudes dropped to about 40 % of their largest value, presumably because of the interactions with the Ekman-vortex structure that is expected to form starting at $1/Ro_c$. For $1/Ro \gtrsim 0.7$ the amplitudes remained more or less constant as $1/Ro$ was increased.

Also shown in the figure are the root-mean-square amplitudes of the temperature fluctuations about the cosine fit. Interestingly, there was an apparently sudden onset of a mild increase which coincided with $1/Ro_c$. For larger rotation rates the fluctuations grew somewhat and near $1/Ro = 0.7$ reached values close to the amplitudes $\langle \delta_k \rangle$. Beyond that point it is difficult for us to be sure about the existence of an LSC without more detailed analysis, even though the time averages of the standard errors of the δ_k (also shown in the figure) remained well below the δ_k themselves.

5.3. *Time-dependence of the large-scale circulation temperature amplitude*

In figure 14(a), we show a time series of δ_m from run E8 in the absence of rotation. One sees that δ_m fluctuates as seen before, and that on rare occasions it briefly vanishes (Brown *et al.* 2005*a*; Brown & Ahlers 2006*b*). These events, where the flow briefly stops, are known as cessations and have been the subject of extensive experimental

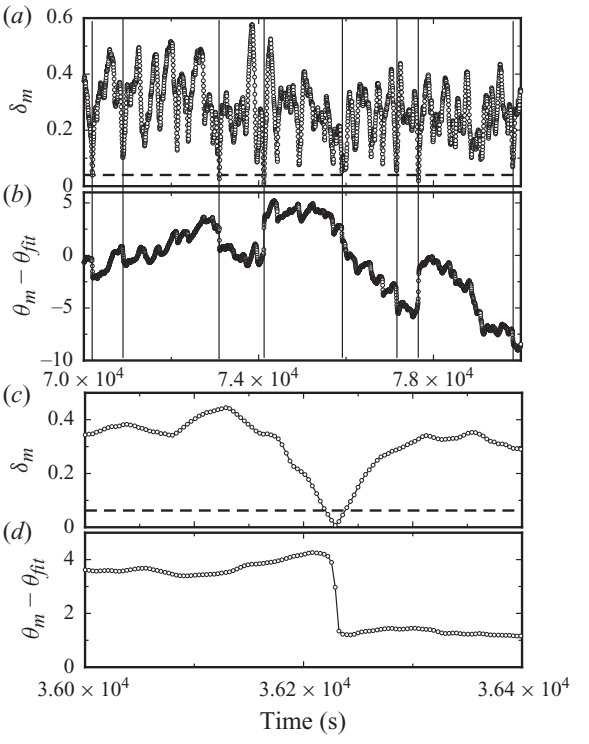

FIGURE 15. (*a*) The temperature amplitude δ_m at the horizontal mid-plane for $Ra = 1.8 \times 10^{10}$, $Pr = 4.38$ and $1/Ro = 0.432$ (run E8) as a function of time. (*b*) The deviation of the azimuthal orientation $\theta_m - \theta_{fit}$ from a straight-line fit $\theta_{fit}(t)$ corresponding to (*a*). The vertical lines are guides to the eye to show the correlation between strong dips in δ_m and sudden jumps in $\theta_m - \theta_{fit}$. (*c*) and (*d*) are detailed illustrations of a cessation for $Ra = 1.8 \times 10^{10}$, $Pr = 4.38$ and $1/Ro = 0.360$.

and theoretical studies. They occur approximately once a day. In order to define a cessation, we require that δ_m decreases below a critical value δ_l. Somewhat arbitrarily δ_l was chosen to be $0.15\langle\delta_m\rangle$ (see e.g. Brown & Ahlers 2006*b* for a discussion of the choice and influence of δ_l); it is indicated by the horizontal dashed line in the figure.

In figure 14(*b*), we show similar data for δ_m, but for the rotating system with $1/Ro = 0.26$, which is still well below the critical value $1/Ro_c \simeq 0.41$. It is immediately clear that the frequency of cessations increased dramatically due to the rotation.

In order to show that the vanishing of the LSC amplitude δ_m is accompanied by the sudden change in the LSC orientation that is typical of cessations, we show another data set in figure 15. Here we compare δ_m (figure 15*a*) with the LSC orientation (figure 15*b*). However, in the rotating system the average retrograde rotation, to be discussed in § 5.4, had to be subtracted before the dynamics of the LSC orientation could be seen. Thus we fit a straight line to $\theta_m(t)$ over a long time interval to obtain θ_{fit}, and plotted $\theta_m - \theta_{fit}$ as a function of time in figure 15(*b*). The vertical lines are guides to the eye, and show that near-discontinuous jumps in the LSC orientation coincided with near-vanishing of δ_m. The jumps in orientation seem to be of randomly different size as found in the absence of rotation, but we have not done a quantitative statistical analysis. In figures 15(*c*) and 15(*d*), we show details of a typical cessation. As expected, the amplitude decreases dramatically, and when it is near its minimum, the LSC orientation changes quite suddenly. We conclude that the qualitative features

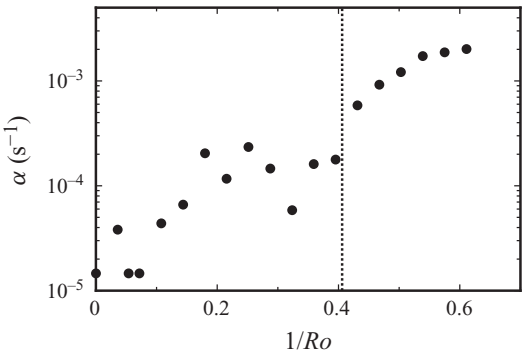

FIGURE 16. Rate of the cessations as function of $1/Ro$. A cessation is said to have occurred when δ_m dropped to less then the threshold value $\delta_l = 0.15 * \langle \delta_m \rangle$. As in figure 14, these data are also for run E8. The transition at $1/Ro_c = 0.406$ is indicated by the vertical dotted line.

of cessations in the presence of rotation are the same as they are for $1/Ro = 0$ (Brown & Ahlers 2006*b*).

In figure 16, we show the average number of cessations α observed at various values of $1/Ro$. One sees that α increased dramatically with $1/Ro$, from near 10^{-5} close to $1/Ro = 0$ to just above 10^{-4} near $1/Ro = 0.2$. Apparently, there was then a plateau which extended up to $1/Ro_c \simeq 0.4$. At $1/Ro_c$ there was a jump in α by a factor of three, followed by a further gradual increase up to a frequency of about once every 500 s near $1/Ro = 0.6$. For even larger $1/Ro$ cessations were so frequent that it became difficult to identify individual events.

5.4. *Retrograde rotation of the large-scale circulation*

The LSC takes place in a near-vertical circulation plane. In the absence of viscous drag, one would expect the orientation of this plane to remain constant in an inertial frame because the LSC has angular momentum (Brown & Ahlers 2006*a*). Consequently, one would expect the orientation θ_0 in the frame of a sample rotating with angular velocity Ω to undergo retrograde rotation at an angular velocity $\omega = -\Omega$. This will be altered by the presence of viscous drag on the walls across the viscous boundary layers, so that in the physical system $|\omega| < |\Omega|$. This phenomenon is contained in a deterministic model by Hart *et al.* (2002), and in more detail in a stochastic model by Brown & Ahlers (2006*a*) that was developed to explain the influence of Earth's Coriolis force on the statistical properties of the LSC. However, measurements by both groups, as well as more recent ones by Kunnen *et al.* (2008*b*), showed that estimates of the drag by the walls based on the ordinary shear viscosity of the fluid were too small and gave values of $-\omega/\Omega$ that were too large (albeit of course less than one). Hart *et al.* (2002) introduced a turbulent viscosity that led to values of $-\omega/\Omega$ that were closer to the experiment.

In figure 17, we show some of our measurements of the orientation θ_0 of the LSC circulation plane as a function of time. The numbers in the figures are the value of $1/Ro$. For $1/Ro = 0$ the data reveal the usual azimuthal diffusion that has been observed before. For $1/Ro > 0$ the retrograde rotation is obvious and on average led to a linear decrease of θ_0 with time. Measurements of $\theta_0(t)$ for $1/Ro > 0$ were also made by Hart *et al.* (2002) and by Kunnen *et al.* (2008*b*). The latter authors found that $\theta(t)$ ceased to follow a linear dependence when $1/Ro \gtrsim 0.2$ or 0.3. They interpreted this to imply that the LSC gradually disappeared as $1/Ro$ increased. Our data continued

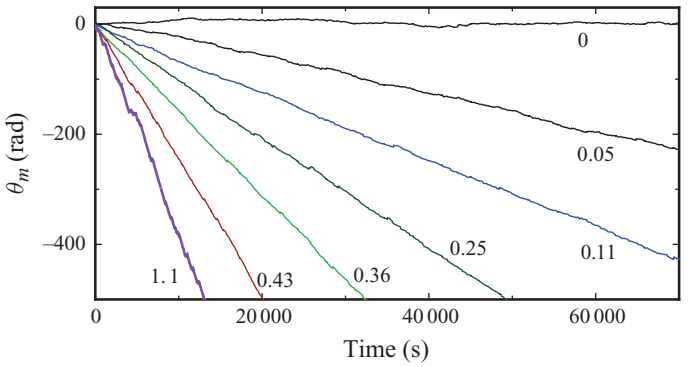

FIGURE 17. (Colour online) The orientation θ_m of the LSC circulation plane as a function of time. The numbers in the figures indicate the values of $1/Ro$. All data are for run E8 with $Ra = 1.8 \times 10^{10}$ and $Pr = 4.38$.

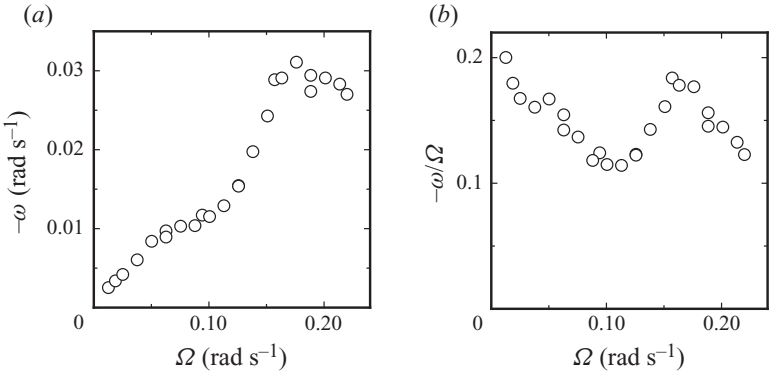

FIGURE 18. (*a*) Retrograde rotation velocity $-\omega$ as function of the sample rotation velocity Ω. (*b*) The ratio $-\omega/\Omega$ as a function of Ω. The data are for run E8 ($Ra = 1.8 \times 10^{10}$, $Pr = 4.38$).

to reveal retrograde rotation up to $1/Ro \simeq 1$. However, for $1/Ro \gtrsim 0.4 \simeq 1/Ro_c$ (see § 3.2.3) the time traces became noisier; but there remained linear trends on average over sufficiently long time intervals as shown by the data in figure 17 that extend up to $1/Ro = 1.1$.

Straight-line fits to data such as those in figure 17 led to the retrograde rotation rates ω that are shown in figure 18(*a*) as a function of Ω and in figure 19(*a*) and c as a function of $1/Ro$. The above-mentioned models (Hart *et al.* 2002; Brown & Ahlers 2006*a*) predicted that ω should be proportional to Ω, i.e. $-\omega/\Omega$ should be independent of Ω or $1/Ro$. They also yielded only a very weak dependence on Ra, and predicted a value only somewhat less than unity for $-\omega/\Omega$. For example, the model of Brown & Ahlers (2006*a*), which assumed viscous drag by the sidewalls based on the ordinary shear viscosity of the fluid, predicted $-\omega/\Omega = 0.77$, 0.83 and 0.85 for runs E6, E7 and E8, respectively. For small rotation rates a linear dependence of ω on Ω was indeed observed within their experimental resolution by Hart *et al.* (2002). A glance at figure 18(*a*) suggests that a linear dependence is also consistent with our data; but closer inspection reveals a more complex behaviour. This is seen in figure 18(*b*) and in figure 19(*b*, *d*), where we show the measured ratios. The data show interesting structure even for $1/Ro < 1/Ro_c$. We note that the most rapid variation with $1/Ro$ occurs in

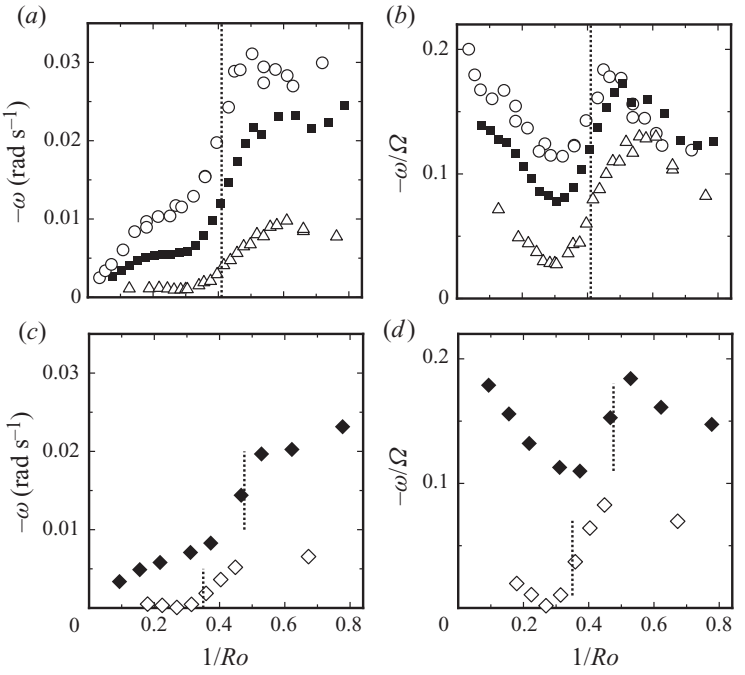

FIGURE 19. (*a*, *c*) Retrograde rotation velocity $-\omega$ as function of the inverse Rossby number $1/Ro$. (*b*, *d*) The ratio $-\omega/\Omega$ as a function of $1/Ro$. The panels (*a*) and (*b*) show the dependence on Ra at nearly constant Pr, and the bottom ones give the dependence on Pr at nearly constant Ra. Open circles, run E8 ($Ra = 1.8 \times 10^{10}$, $Pr = 4.38$). Solid squares, run E7 ($Ra = 9.0 \times 10^{9}$, $Pr = 4.38$). Open triangles, run E6 ($Ra = 2.2 \times 10^{9}$, $Pr = 4.38$). Solid diamonds, run E11 ($Ra = 8.0 \times 10^{9}$, $Pr = 3.05$). Open diamonds, run E3 ($Ra = 2.2 \times 10^{9}$, $Pr = 6.26$). The vertical dotted lines indicate the location of $1/Ro_c$ as determined from the Nusselt-number measurements.

the region near $1/Ro_c$, and that no singularity is apparent at that bifurcation. This is not unlike the behaviour of $\langle \delta_k \rangle$ shown in figure 13. Figure 19(*a*, *b*) shows that $-\omega/\Omega$ increases as Ra increases when Pr is constant. Similarly, figure 19(*c*, *d*) shows that, at constant Ra, the ratio increases as Pr decreases. If we try to match the predictions of the models to the data by introducing an effective turbulent viscosity, then this viscosity would need to have non-trivial dependences on $1/Ro$, Pr and Ra even at these small rotation rates. Clearly there remains much of interest to be understood.

6. Summary and discussion

A major emphasis of much of the work on rotating turbulent RBC has been on the global heat transport. As reported briefly elsewhere (Zhong *et al.* 2009) and found by several other authors (Rossby 1969; Zhong *et al.* 1993; Liu & Ecke 1997*b*; Kunnen *et al.* 2006, 2008*b*; Liu & Ecke 2009), we found that rotation at modest rates can enhance the heat transport (see figures 4, 5 and 8), rather than suppressing it as expected on the basis of the TP effect and as seen close to the onset of convection (Chandrasekhar 1981). Over our parameter range we found that this enhancement can be up to about 20 %, but the DNS of Stevens *et al.* (2010*b*) showed that it can be as large as 30 % when Ra is near 10^8 and Pr is near 20 or so. The enhancement is now understood to be caused by Ekman vortices that form due to the

rotation (Boubnov & Golitsyn 1986, 1990; Hart 1995, 2000; Julien *et al.* 1996*b*, 1999; Vorobieff & Ecke 1998, 2002; Hart *et al.* 2002; Kunnen *et al.* 2006; Zhong *et al.* 2009; Stevens 2010*b*); the vortex cores extract additional fluid out of the thermal BLs and thereby enhance the heat transport. We presented quantitative measurements of this effect as a function of Pr and Ra. It should be noted that there are also experiments (Pfotenhauer *et al.* 1984; Niemela *et al.* 2010) that, for certain Γ, Pr and Ra, did not reveal any enhancement of Nu. Thus it remains to understand in detail the parameter ranges over which enhancement occurs.

Quite remarkably, the enhancement of Nu did not start at $1/Ro = 0$, but rather occurred only above a finite threshold rotation rate $1/Ro_c$ (Stevens *et al.* 2009) (see figures 4 and 5). This threshold decreased mildly with increasing Pr, but seemed essentially independent of Ra over our parameter range (see figure 6). At the threshold the enhancement of Nu started continuously from zero, consistent with a supercritical bifurcation. Bifurcations between turbulent states are somewhat unexpected because the highly fluctuating systems are presumed to already sample all of the available phase space; when bifurcations do occur, then they are most likely associated either with changes in the boundary conditions (or BLs) or in relevant large-scale structures. Consistent with these general considerations, we interpret the observed bifurcation as a transition from a turbulent state without to one with Ekman pumping, i.e. to a discontinuous onset of the formation of large-scale structures in the form of Ekman vortices; but we do not understand why that formation should have a finite threshold.

Close to but above $1/Ro_c$ the Ekman-pumping enhancement of Nu, as measured by the initial slope S_1 of $Nu(1/Ro)$ just above $1/Ro_c$, became larger with increasing Pr, but only by just under 20 % over our Pr range from 3.0 to 6.4 (see figure 7). The data did not reveal any significant dependence of S_1 on Ra. The smaller enhancement at smaller Pr was attributed by Zhong *et al.* (2009) to the larger thermal diffusivity, which promotes lateral heat exchange and thereby tends to reduce the pumping efficiency of the Ekman vortices. It was suggested by Stevens *et al.* (2010*b*) that, with increasing Pr, there is a Pr value of maximum enhancement because at very large Pr the viscous BLs become so thick that the Ekman vortices no longer have access to the thermal BLs, where the enhanced heat transport originates. Our measurements did not extend to this large Pr regime, and experiments or DNS that reveal a maximum of S_1 as a function of Pr at constant Ra, to our knowledge, have not yet been performed. However, at constant $1/Ro = 1$, where one would expect the TP suppression to still be very small, Stevens *et al.* (2010*b*) showed from DNS that $Nu(1/Ro)/Nu(0)$ has a maximum near $Pr = 10$.

We do not know of a rigorous way to separate the Ekman enhancement and the TP suppression of the Nusselt number; but the data do suggest a natural separation. One finds that the curves for $Nu(1/Ro)/Nu(0)$ versus $1/Ro$ start out with a common Ra independent but weakly Pr-dependent monotonically increasing envelope, but then fall away to lower values at a dramatic rate, starting at different values of $1/Ro$ that depend on Ra and Pr. This is illustrated well in figures 4 and 5, and we demonstrate it further in figure 20, which shows all of our data. There the solid line is an empirical power-law fit to the data from run E2 for $0.5 \lesssim 1/Ro \lesssim 4$. Similar envelopes could be drawn for each Pr, and would differ only slightly from the one shown in the figure. The data thus suggest that their natural interpretation is to attribute the common envelope to an only weakly Pr-dependent and Ra-independent Ekman enhancement, and the depression below it to a strongly Pr- and Ra-dependent TP suppression. This interpretation implies that at constant Ra the depression becomes more severe as the Prandtl number decreases, and that at constant Pr it becomes larger at larger

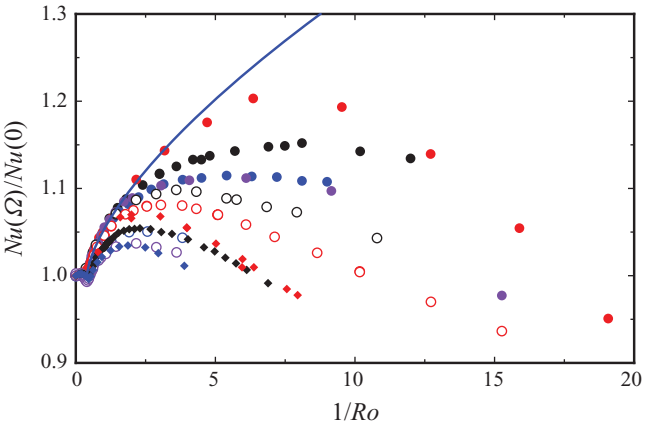

FIGURE 20. (Colour online) All of the data for $y = Nu(1/Ro)/Nu(0)$ as a function of $x = 1/Ro$ on linear scales. Solid black circles: E1; solid red circles: E2; solid blue circles: E3; solid purple circles: E4; open black circles: E5; open red circles: E6; open blue circles: E7; open purple circles: E8; solid black diamonds: E9; solid red diamonds: E10; solid blue diamonds: E11. The solid line is the power law $y = y_0 + m(x - x_0)^{\zeta}$ with $y_0 = 1$, $x_0 = 0.4$, $m = 0.074$ and $\zeta = 0.66$ obtained from fitting the E2 data for $0.5 \lesssim 1/Ro \lesssim 4$.

Ra. It is then the competition between this TP reduction and the Ekman enhancement that determines the strong Pr- and Ra-dependence of the Nu enhancement near the maximum of $Nu(1/Ro)$. An alternative to this interpretation would imply that the Ekman enhancement becomes less efficient as $1/Ro$ increases, thus leading to the maximum in the data. This alternative seems unlikely to us.

Qualitatively we can understand the strong Pr-dependence at constant Ra and $1/Ro$ displayed in figure 8(a) by considering the variation of the Ekman number Ek, which represents the ratio of the strength of the viscous force to that of the Coriolis force. Along a vertical line in the figure Ek increases with increasing Pr (see also table 1). Thus viscous dissipation, which suppresses the TP effect, increases (relative to the Coriolis force) as Pr increases at constant Ra and $1/Ro$, thereby diminishing the Nu enhancement by the TP effect.

A second important topic is the influence of rotation on the LSC. The LSC has several properties with interesting dependences on $1/Ro$ that we investigated and briefly describe below.

In the absence of rotation, plumes emitted by the top and bottom thermal BLs are swept by the LSC and travel vertically mostly near the sidewall. There they generate a destabilizing vertical thermal gradient that is much larger than the very small gradient along the axis of the system (Brown & Ahlers 2007b). We found that these gradients initially were diminished as $1/Ro$ increased from zero. They reached a minimum somewhat below $1/Ro_c$, followed by an increase until a strong enhancement was reached at large $1/Ro$ (see figures 10 and 11). There the enhancement was larger for larger Pr at constant Ra, and larger for larger Ra at constant Pr; compared to its value at $1/Ro = 0$, it reached a factor of 2.5 for some parameters. The strong enhancement presumably was associated with contributions from the Ekman-vortex structures; but the depression of the gradient below $1/Ro_c$ remains to be explained.

In the absence of rotation, the Reynolds number Re of the LSC has often been determined from the frequency of oscillations detected by various experimental

techniques (Ahlers *et al.* 2009). We determined Re from oscillations in auto-correlation functions of sidewall temperature measurements (see figure 12*b*) and found that Re was initially unchanged within our resolution as $1/Ro$ increased, up to about $1/Ro = 0.3$ (see figure 12*c*). With further increase of $1/Ro$, it decreased, but we were unable to make measurements for $1/Ro \gtrsim 0.5$ because enhanced fluctuations of the system prevented the resolution of the correlation-function oscillations. The constant values of Re stand in contrast to the strong decrease of the thermal gradient along the wall and to the strong increase of the LSC temperature amplitudes $\langle \delta_k \rangle$ to be discussed below.

An important issue is whether the LSC continues to exist as $1/Ro$ increases, or whether the evolving Ekman-vortex structure and associated vigorous temperature and velocity fluctuations lead to the complete destruction of the LSC as was concluded by some previous investigators (Hart *et al.* 2002; Kunnen *et al.* 2008*b*). From the analyses of time series of sidewall temperature measurements, we found that the LSC continued to exist up to $1/Ro \simeq 1$, but for larger $1/Ro$ the temperature fluctuations became too severe and the LSC amplitudes became too small for us to be sure of the LSC existence.

Remarkably, the time-averaged thermal amplitude $\langle \delta_k \rangle$ first increased with increasing $1/Ro$, but for $1/Ro \gtrsim 0.3$ it decreased and for $1/Ro \gtrsim 0.6$ it settled down at a near-constant value which was still about 60 or 70 % of its value in the absence of rotation (see figure 13*b*). Interestingly, there was no obvious singularity in $\langle \delta_k \rangle$ at $1/Ro_c$. However, the LSC became obscured by fluctuations that grew by a factor of 2 or so as $1/Ro$ grew from 0 to greater than 1.

It is well known that for the non-rotating system the LSC undergoes rare cessations of its flow when $\langle \delta_k \rangle$ vanishes (Brown *et al.* 2005*a*; Brown & Ahlers 2006*b*). We found that the frequency of cessations was dramatically enhanced by even modest rotation (see figures 14 and 16). The cessation frequency increased from about $10^{-5}\,\mathrm{s}^{-1}$ for $1/Ro = 0$ to about $1.5 \times 10^{-4}\,\mathrm{s}^{-1}$ for $1/Ro = 0.2$. At $1/Ro_c$ there was a jump by a factor of about 3 in the cessation rate. These are interesting experimental observations, but like many other features of this system, they remain unexplained.

Finally, an intriguing aspect of this system is the retrograde rotation rate ω of the orientation of the LSC circulation plane. In the absence of dissipation, one would expect $\omega = -\Omega$ because the system has angular momentum and thus an orientation that, in the absence of an applied torque, should remain steady in an inertial frame. Small deviations from this, with $-\omega/\Omega \simeq 0.8$, are expected due to viscous drag on the sample walls (Hart *et al.* 2002; Brown & Ahlers 2006*a*, 2008*a*). However, typical measurements yielded $-\omega/\Omega \lesssim 0.2$ (see figure 19). One would be tempted to invoke a turbulent viscosity to explain this larger drag, as was done by Hart *et al.* (2002). However, there is intricate structure of ω/Ω as a function of $1/Ro$ in the range $1/Ro \lesssim 0.7$ or so that would then imply a similar structure of this turbulent viscosity, which would need to be explained.

All of the properties displayed in figures 11–19 show significant and intriguing structure at small $1/Ro$. In order to see whether there is any correlation between particular features of different properties, we show all of them for $Ra = 9.0 \times 10^9$ and $Pr = 4.38$ in figure 21 on the same horizontal scale. There the vertical dotted line is $1/Ro_c$ as determined from the Nusselt measurements. In figure 21(*a*), we also demonstrate the method of determining $1/Ro_c$ by the two solid lines which are fits to data subsets below and above the transition. The vertical short dashed line passes through the maximum of the LSC thermal amplitude $\langle \delta_m \rangle$ shown in figure 21(*d*). This point coincides with the value of $1/Ro$, where the slope of the vertical temperature

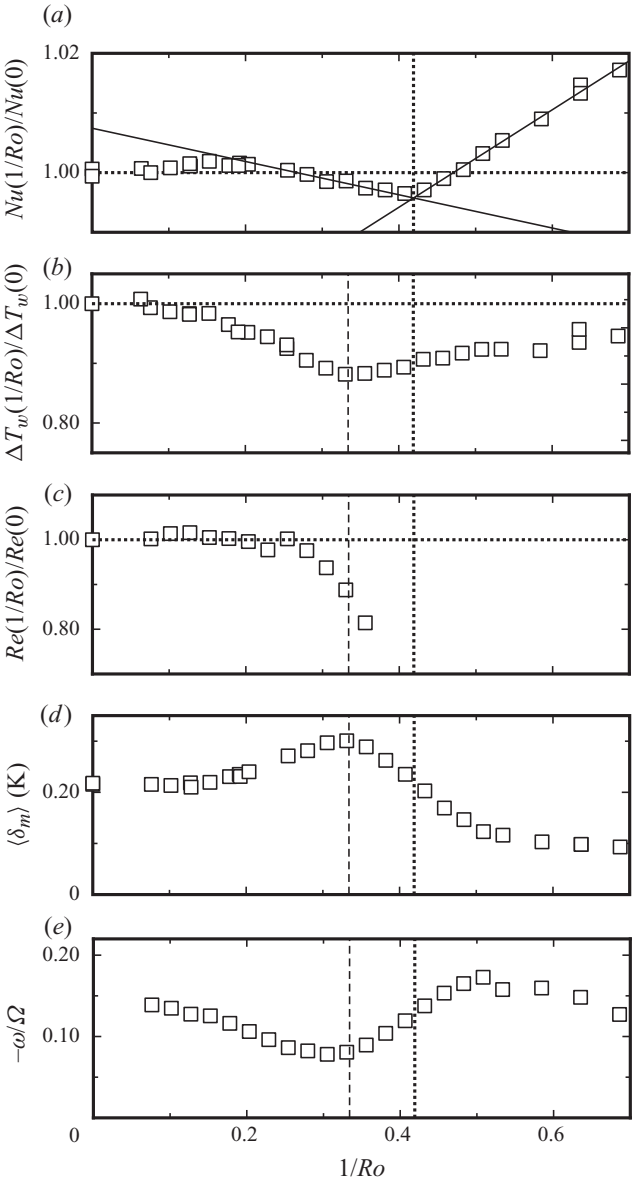

FIGURE 21. (*a*) The excess Nusselt number $Nu(1/Ro)/Nu(0)$; (*b*) the vertical thermal gradient $\Delta T_w(1/Ro)/\Delta T_w(0)$ near the sidewall; (*c*) the reduced Reynolds number $Re(1/Ro)/Re(0)$; (*d*) the thermal LSC amplitude $\langle \delta_m \rangle$; and (*e*) the retrograde rotation rate $-\omega/\Omega$ of the LSC. All are shown on the same horizontal scale as a function of $1/Ro$ and are for $Pr = 4.38$ and $Ra = 9.0 \times 10^9$.

gradient $\Delta T_w(Ro)/\Delta T_w(0)$ (figure 21*b*) changes more or less abruptly. However, the Reynolds number shown in figure 21(*c*) begins to drop earlier and shows no remarkable behaviour at that point. The minimum of the retrograde rotation rate, shown in figure 21(*e*), occurs slightly below and not at the vertical dashed line. The apparent correlation between $\Delta T_w(Ro)/\Delta T_w(0)$ and $\langle \delta_m \rangle$ may indeed be significant because one would expect a more vigorous LSC to lead to lesser vertical temperature

gradients; but it is surprising that neither of these properties shows any anomaly at $1/Ro_c$. It is difficult to see any significant correlation between the behaviour of $Re(\Omega)/Re(0)$ or $-\omega/\Omega$ and the other properties, but again it is noteworthy that these last two also pass smoothly through $1/Ro_c$. It seems that the presumed onset of Ekman-vortex formation at $1/Ro_c$ does not have a large effect on the various properties of the LSC.

There still remain numerous issues that are inadequately studied by experiment or DNS. Among them is the absence of a bifurcation as a function of $1/Ro$ for $Ra \simeq 4 \times 10^7$ (Stevens *et al.* 2010*a*), while such a bifurcation exists for $Ra \gtrsim 10^8$ (Stevens *et al.* 2009). One would like to know whether this transition occurs by virtue of a vanishing slope $S_1(Ra)$ of $Nu(1/Ro)$ at a critical value Ra^* of Ra. In view of the data in figure 7, this seems unlikely, and in any case, it would require an explanation of the existence of yet another bifurcation, this time as a function of Ra. Instead, one might like to know whether the bifurcation as a function of $1/Ro$ disappears discontinuously, with finite S_1 above and $S_1 = 0$ below a transition at some Ra^* in the range $4 \times 10^7 \lesssim Ra^* \lesssim 10^8$. This too would correspond to a bifurcation along the Ra axis, and presumably would be related to a discontinuous change in the nature of the turbulent state of RBC without rotation as Ra drops below about 10^8 or so (see e.g. Heslot, Castaing & Libchaber 1987). Alternatively, one might ask whether S_1 simply becomes sufficiently small with decreasing Ra to be no longer resolved by the DNS. This question could in principle be answered by DNS or experiments at closely spaced values of Ra that would extend the data for S_1 in figure 7 to smaller values of Ra. Similarly, one would like to know in more detail the parameter ranges at small Pr or large Ra over which the Ekman enhancement disappears for any Ro (Zhong *et al.* 2009; Niemela *et al.* 2010).

Even more issues are awaiting a theoretical explanation. Prominent among these are the $1/Ro$-dependences of several properties at relatively small $1/Ro \lesssim 0.5$ or so. These properties include the Nusselt number, the vertical thermal gradient near the sidewall, the LSC Reynolds number, the LSC thermal amplitude $\langle \delta_k \rangle$, the size of the temperature fluctuations about the azimuthal sinusoidal temperature profile along the sidewall, the frequency of cessations of the LSC and the retrograde rotation rate of the LSC. Equally important would be an explanation of the very existence of a bifurcation, rather than a continuous evolution towards the Ekman state. A quantitative treatment of the size of the Ekman enhancement and of the TP depression of the heat transport likewise seems to be lacking at this time. It is apparent that much remains to be done on this problem.

We benefitted from numerous discussions with, and comments on an early version of this manuscript by H. J. H. Clercx, D. Lohse, and R. J. A. M. Stevens, and from comparisons of our results with their DNS results. This work was supported by the US National Science Foundation through Grant DMR07-02111. One of us (G.A.) is grateful to the Alexander von Humboldt Foundation for support and to the Max Planck Institute for Dynamics and Self-organization for their hospitality while this paper was in preparation.

REFERENCES

Ahlers, G. 2009 Turbulent convection. *Physics* **2**, 74.

Ahlers, G., Brown, E., Fontenele Araujo, F., Funfschilling, D., Grossmann, S. & Lohse, D. 2006*a* Non-Oberbeck–Boussinesq effects in strongly turbulent Rayleigh–Bénard convection. *J. Fluid Mech.* **569**, 409–445.

Ahlers, G., Brown, E. & Nikolaenko, A. 2006*b* The search for slow transients, and the effect of imperfect vertical alignment, in turbulent Rayleigh–Bénard convection. *J. Fluid Mech.* **557**, 347–367.

Ahlers, G., Grossmann, S. & Lohse, D. 2002 Hochpräzision im Kochtopf: neues zur turbulenten Konvektion. *Phys. J.* **1** (2), 31–37.

Ahlers, G., Grossmann, S. & Lohse, D. 2009 Heat transfer and large scale dynamics in turbulent Rayleigh–Bénard convection. *Rev. Mod. Phys.* **81**, 503–538.

Ahlers, G. & Xu, X. 2001 Prandtl-number dependence of heat transport in turbulent Rayleigh–Bénard convection. *Phys. Rev. Lett.* **86**, 3320–3323.

Bajaj, K., Ahlers, G. & Pesch, W. 2002 Rayleigh–Bénard convection with rotation at small Prandtl numbers. *Phys. Rev.* E **65**, 056309.

Bajaj, K. M. S., Liu, J., Naberhuis, B. & Ahlers, G. 1998 Square patterns in Rayleigh–Bénard convection with rotation about a vertical axis. *Phys. Rev. Lett.* **81**, 806–809.

Becker, N. & Ahlers, G. 2006*a* The domain chaos puzzle and the calculation of the structure factor and its half-width. *Phys. Rev.* E **73**, 046209.

Becker, N. & Ahlers, G. 2006*b* Local wave director analysis of domain chaos in Rayleigh–Bénard convection. *J. Stat. Mech.* **P12002**, 1–39.

Becker, N., Scheel, J., Cross, M. & Ahlers, G. 2006 Effect of the centrifugal force on domain chaos in Rayleigh–Bénard convection. *Phys. Rev.* E **73**, 066309.

Bodenschatz, E., Cannell, D. S., de Bruyn, J., Ecke, R., Hu, Y., Lerman, K. & Ahlers, G. 1992 Experiments on three systems with non-variational aspects. *Physica* D **61**, 77–93.

Boubnov, B. M. & Golitsyn, G. S. 1986 Experimental study of convective structures in rotating fluids. *J. Fluid Mech.* **167**, 503–531.

Boubnov, B. M. & Golitsyn, G. S. 1990 Temperature and velocity field regimes of convective motions in a rotating plane fluid layer. *J. Fluid Mech.* **219**, 215–239.

Brown, E. & Ahlers, G. 2006*a* Effect of the Earth's Coriolis force on turbulent Rayleigh–Bénard convection in the laboratory. *Phys. Fluids* **18**, 125108.

Brown, E. & Ahlers, G. 2006*b* Rotations and cessations of the large-scale circulation in turbulent Rayleigh–Bénard convection. *J. Fluid Mech.* **568**, 351–386.

Brown, E. & Ahlers, G. 2007*a* Large-scale circulation model of turbulent Rayleigh–Bénard convection. *Phys. Rev. Lett.* **98**, 134501.

Brown, E. & Ahlers, G. 2007*b* Temperature gradients and search for non-Boussinesq effects in the interior of turbulent Rayleigh–Bénard convection. *Europhys. Lett.* **80**, 14001.

Brown, E. & Ahlers, G. 2008*a* Azimuthal asymmetries of the large-scale circulation in turbulent Rayleigh–Bénard convection. *Phys. Fluids* **20**, 105105.

Brown, E. & Ahlers, G. 2008*b* A model of diffusion in a potential well for the dynamics of the large-scale circulation in turbulent Rayleigh–Bénard convection. *Phys. Fluids* **20**, 075101.

Brown, E. & Ahlers, G. 2009 The origin of oscillations of the large-scale circulation of turbulent Rayleigh–Bénard convection. *J. Fluid Mech.* **638**, 383–400.

Brown, E., Funfschilling, D. & Ahlers, G. 2007 Anomalous Reynolds-number scaling in turbulent Rayleigh–Bénard convection. *J. Stat. Mech.* **2007**, P10005.

Brown, E., Nikolaenko, A. & Ahlers, G. 2005*a* Reorientation of the large-scale circulation in turbulent Rayleigh–Bénard convection. *Phys. Rev. Lett.* **95**, 084503.

Brown, E., Nikolaenko, A., Funfschilling, D. & Ahlers, G. 2005*b* Heat transport by turbulent Rayleigh–Bénard convection: effect of finite top- and bottom-plate conductivity. *Phys. Fluids* **17**, 075108.

Buell, J. C. & Catton, I. 1983 Effect of rotation on the stability of a bounded cylindrical layer of fluid heated from below. *Phys. Fluids* **26**, 892–896.

Busse, F. H. 1994 Convection driven zonal flows and vortices in the major planets. *Chaos* **4**, 123–134.

Busse, F. H. & Heikes, K. E. 1980 Convection in a rotating layer: a simple case of turbulence. *Science* **208**, 173–175.

Chandrasekhar, S. 1981 *Hydrodynamic and Hydromagnetic Stability*. Dover.

Choi, W., Prasad, D., Camassa, R. & Ecke, R. 2004 Traveling waves in rotating Rayleigh–Bénard convection. *Phys. Rev.* E **69**, 056301.

Ciliberto, S., Cioni, S. & Laroche, C. 1996 Large-scale flow properties of turbulent thermal convection. *Phys. Rev.* E **54**, R5901–R5904.

Cioni, S., Ciliberto, S. & Sommeria, J. 1997 Strongly turbulent Rayleigh–Bénard convection in mercury: comparison with results at moderate Prandtl number. *J. Fluid Mech.* **335**, 111–140.

Clever, R. M. & Busse, F. H. 1979 Nonlinear properties of convection rolls in a horizontal layer rotating about a vertical axis. *J. Fluid Mech.* **94**, 609–627.

Ecke, R. E., Zhong, F. & Knobloch, E. 1992 Hopf bifurcation with broken reflection symmetry in rotating Rayleigh–Bénard convection. *Europhys. Lett.* **19**, 177–182.

Fantz, M., Friedrich, R., Bestehorn, M. & Haken, H. 1992 Pattern formation in rotating Bénard convection. *Physica* D **61**, 147–154.

Fernando, H. J. S., Chen, R. & Boyer, D. L. 1991 Effects of rotation on convective turbulence. *J. Fluid Mech.* **228**, 513–547.

Funfschilling, D. & Ahlers, G. 2004 Plume motion and large scale circulation in a cylindrical Rayleigh–Bénard cell. *Phys. Rev. Lett.* **92**, 194502.

Funfschilling, D., Brown, E. & Ahlers, G. 2008 Torsional oscillations of the large-scale circulation in turbulent Rayleigh–Bénard convection. *J. Fluid Mech.* **607**, 119–139.

Funfschilling, D., Brown, E., Nikolaenko, A. & Ahlers, G. 2005 Heat transport by turbulent Rayleigh–Bénard convection in cylindrical cells with aspect ratio one and larger. *J. Fluid Mech.* **536**, 145–154.

Gascard, J., Watson, A., Messias, M., Olsson, K., Johannessen, T. & Simonsen, K. 2002 Long-lived vortices as a mode of deep ventilation in the Greenland Sea. *Nature (London)* **416**, 525–527.

Glatzmaier, G., Coe, R., Hongre, L. & Roberts, P. 1999 The role of the Earth's mantle in controlling the frequency of geomagnetic reversals. *Nature (London)* **401**, 885–890.

Grossmann, S. & Lohse, D. 2000 Scaling in thermal convection: a unifying view. *J. Fluid. Mech.* **407**, 27–56.

Grossmann, S. & Lohse, D. 2001 Thermal convection for large Prandtl number. *Phys. Rev. Lett.* **86**, 3316–3319.

Hart, J. E. 1995 Nonlinear Ekman suction and agesotrophic effects in rapidly rotating flows. *Geophys. Astrophys. Fluid Dyn.* **79**, 201–222.

Hart, J. E. 2000 A note on nonlinear corrections to the Ekman layer pumping velocity. *Phys. Fluids* **12**, 131–135.

Hart, J. E., Kittelman, S. & Ohlsen, D. R. 2002 Mean flow precession and temperature probability density functions in turbulent rotating convection. *Phys. Fluids* **14**, 955–962.

Hart, J. E. & Olsen, D. R. 1999 On the thermal offset in turbulent rotating convection. *Phys. Fluids* **11**, 2101–2107.

Heikes, K. E. & Busse, F. H. 1980 Weakly nonlinear turbulence in a rotating convection layer. *Ann. N.Y. Acad. Sci.* **357**, 28–36.

Heslot, F., Castaing, B. & Libchaber, A. 1987 Transition to turbulence in helium gas. *Phys. Rev.* A **36**, 5870–5873.

Hu, Y., Ecke, R. & Ahlers, G. 1995 Time and length scales in rotating Rayleigh–Bénard convection. *Phys. Rev. Lett.* **74**, 5040–5043.

Hu, Y., Ecke, R. E. & Ahlers, G. 1997 Convection under rotation for Prandtl numbers near one: linear stability, wavenumber selection, and pattern dynamics. *Phys. Rev.* E **55**, 6928–6949.

Hu, Y., Pesch, W., Ahlers, G. & Ecke, R. E. 1998 Convection under rotation for Prandtl numbers near one: Küppers–Lortz instability. *Phys. Rev.* E **58**, 5821–5833.

Jones, C. 2000 Convection-driven geodynamo models. *Phil. Trans. R. Soc. Lond.* A **358**, 873–897.

Julien, K., Legg, S., McWilliams, J. & Werne, J. 1996*a* Hard turbulence in rotating Rayleigh–Bénard convection. *Phys. Rev.* E **53**, R5557–R5560.

Julien, K., Legg, S., McWilliams, J. & Werne, J. 1996*b* Rapidly rotating turbulent Rayleigh–Bénard convection. *J. Fluid Mech.* **322**, 243–273.

Julien, K., Legg, S., McWilliams, J. & Werne, J. 1999 Plumes in rotating convection. Part 1. Ensemble statistics and dynamical balances. *J. Fluid Mech.* **391**, 151–187.

Kadanoff, L. P. 2001 Turbulent heat flow: structures and scaling. *Phys. Today* **54** (8), 34–39.

King, E., Stellmach, S., Noir, J., Hansen, U. & Aurnou, J. 2009 Boundary layer control of rotating convection systems. *Nature* **457**, 301–304.

Kunnen, R. P. J., Clercx, H. J. H. & Geurts, B. J. 2006 Heat flux intensification by vortical flow localization in rotating convection. *Phys. Rev.* E **74**, 056306.

Kunnen, R., Clercx, H. & Geurts, B. 2008*a* Enhanced vertical inhomogeneity in turbulent rotating convection. *Phys. Rev. Lett.* **101**, 174501.

Kunnen, R. P. J., Clercx, H. J. H. & Geurts, B. J. 2008*b* Breakdown of large-scale circulation in turbulent rotating convection. *Europhys. Lett.* **84**, 24001.

Kunnen, R., Geurts, B. & Clercx, H. 2010 Experimental and numerical investigation of turbulent convection in a rotating cylinder. *J. Fluid Mech.* **642**, 445–476.

Küppers, G. 1970 The stability of steady finite amplitude convection in a rotating fluid layer. *Phys. Lett.* **32A**, 7–8.

Küppers, G. & Lortz, D. 1969 Transition from laminar convection to thermal turbulence in a rotating fluid layer. *J. Fluid Mech.* **35**, 609–620.

Liu, Y. & Ecke, R. 1997*a* Eckhaus–Benjamin–Feir instability in rotating convection. *Phys. Rev. Lett.* **78**, 4391–4394.

Liu, Y. & Ecke, R. 1997*b* Heat transport scaling in turbulent Rayleigh–Bénard convection: effects of rotation and Prandtl number. *Phys. Rev. Lett.* **79**, 2257–2260.

Liu, Y. & Ecke, R. 1999 Nonlinear traveling waves in rotating Rayleigh–Bénard convection: stability boundaries and phase diffusion. *Phys. Rev.* E **59**, 4091–4105.

Liu, Y. & Ecke, R. 2009 Heat transport measurements in turbulent rotating Rayleigh–Bénard convection. *Phys. Rev.* E **80**, 036314.

Lohse, D. & Xia, K.-Q. 2010 Small-scale properties of turbulent Rayleigh–Bénard convection. *Annu. Rev. Fluid Mech.* **42**, 335–364.

Lucas, P., Pfotenhauer, J. & Donnelly, R. 1983 Stability and heat transfer of rotating cryogens. Part 1. Influence of rotation on the onset of convection in liquid ^{4}He. *J. Fluid Mech.* **129**, 251–264.

Marshall, J. & Schott, F. 1999 Open-ocean convection: observations, theory and models. *Rev. Geophys.* **37**, 1–64.

Miesch, M. S. 2000 The coupling of solar convection and rotation. *Solar Phys.* **192**, 59–89.

Millán-Rodríguez, J., Bestehorn, M., Pérez-García, C., Friedrich, R. & Neufeld, M. 1995 Defect motion in rotating fluids. *Phys. Rev. Lett.* **74**, 530–533.

Mishra, P., De, A., Verma, M. & Eswaran, V. 2010 Dynamics of reorientations and reversals of large scale flow in Rayleigh–Bénard convection. *J. Fluid Mech.*, in press (arXiv:1003.2102v4).

Neufeld, M., Friedrich, R. & Haken, H. 1993 Order parameter equation and model equation for high Prandtl number Rayleigh–Bénard convection in a rotating large aspect ratio system. *Z. Phys.* B **92**, 243–256.

Niemela, J., Babuin, S. & Sreenivasan, K. 2010 Turbulent rotating convection at high Rayleigh and Taylor numbers. *J. Fluid Mech.* **649**, 509–522.

Niemela, J. & Donnelly, R. 1986 Direct transition to turbulence in rotating Bénard convection. *Phys. Rev. Lett.* **57**, 2524–2527.

Nikolaenko, A., Brown, E., Funfschilling, D. & Ahlers, G. 2005 Heat transport by turbulent Rayleigh–Bénard convection in cylindrical cells with aspect ratio one and less. *J. Fluid Mech.* **523**, 251–260.

Ning, L. & Ecke, R. 1993*a* Küppers–Lortz transition at high dimensionless rotation rates in rotating Rayleigh–Bénard convection. *Phys. Rev.* E **47**, R2991–R2994.

Ning, L. & Ecke, R. 1993*b* Rotating Rayleigh-Bénard convection: aspect-ratio dependence of the initial bifurcations. *Phys. Rev.* E **47**, 3326–3333.

Pfotenhauer, J. M., Lucas, P. G. J. & Donnelly, R. J. 1984 Stability and heat transfer of rotating cryogens. Part 2. Effects of rotation on heat-transfer properties on convection in liquid ^{4}He. *J. Fluid Mech.* **145**, 239–252.

Pfotenhauer, J., Niemela, J. & Donnelly, R. 1987 Stability and heat-transfer of rotating cryogens. Part 3. Effects of finite cylindrical geometry and rotation on the onset of convection. *J. Fluid Mech.* **175**, 85–96.

Ponty, Y., Passot, T. & Sulem, P. 1997 Chaos and structures in rotating convection at finite Prandtl number. *Phys. Rev. Lett.* **79**, 71–74.

Qiu, X. L. & Tong, P. 2002 Temperature oscillations in turbulent Rayleigh–Bénard convection. *Phys. Rev.* E **66**, 026308.

Roche, P. E., Castaing, B., Chabaud, B. & Hebral, B. 2002 Prandtl and Rayleigh numbers dependences in Rayleigh–Bénard convection. *Europhys. Lett.* **58**, 693–698.

Rossby, H. T. 1969 A study of Bénard convection with and without rotation. *J. Fluid Mech.* **36**, 309–335.

Rubio, A., Lopez, J. & Marques, F. 2010 Onset of Küppers–Lortz-like dynamics in finite rotating thermal convection. *J. Fluid Mech.* **644**, 337–357.

Sakai, S. 1997 The horizontal scale of rotating convection in the geostrophic regime. *J. Fluid Mech.* **333**, 85–95.

Sánchez-Álvarez, J., Serre, E., del Arco, E. C. & Busse, F. 2005 Square patterns in rotating Rayleigh–Bénard convection. *Phys. Rev.* E **72**, 036307.

Scheel, J., Mutyaba, P. & Kimmel, T. 2010 Patterns in rotating Rayleigh-Bénard convection at high rotation rates. *J. Fluid Mech.* (in press).

Schmitz, S. & Tilgner, A. 2009 Heat transport in rotating convection without Ekman layers. *Phys. Rev.* E **80**, 015305.

Stevens, R., Clercx, H. & Lohse, D. 2010*a* Boundary layers in rotating weakly turbulent Rayleigh–Bénard convection. *Phys. Fluids* **22**, 085103.

Stevens, R., Clercx, H. & Lohse, D. 2010*b* Optimal Prandtl number for heat transfer enhancement in rotating turbulent Rayleigh–Bénard convection. *New J. Phys.* **12**, 075005.

Stevens, R., Zhong, J.-Q., Clercx, H., Ahlers, G. & Lohse, D. 2009 Transitions between turbulent states in rotating Rayleigh–Bénard convection. *Phys. Rev. Lett.* **103**, 024503.

Sun, C., Xi, H. D. & Xia, K. Q. 2005 Azimuthal symmetry, flow dynamics, and heat transport in turbulent thermal convection in a cylinder with an aspect ratio of 0.5. *Phys. Rev. Lett.* **95**, 074502.

Thompson, K., Bajaj, K. & Ahlers, G. 2002 Traveling concentric-roll patterns in Rayleigh–Bénard convection with modulated rotation. *Phys. Rev.* E **65**, 046218.

Tilgner, A., Belmonte, A. & Libchaber, A. 1993 Temperature and velocity profiles of turbulence convection in water. *Phys. Rev.* E **47**, R2253–R2256.

Tritton, D. J. 1988 *Physical Fluid Dynamics*. Oxford University Press.

Tu, Y. & Cross, M. 1992 Chaotic domain structure in rotating convection. *Phys. Rev. Lett.* **69**, 2515.

Veronis, G. 1966 Motions at subcritical values of the Rayleigh number in a rotating fluid. *J. Fluid Mech.* **24**, 545–554.

Veronis, G. 1968 Large-amplitude Bénard convection in a rotating fluid. *J. Fluid Mech.* **31**, 113–139.

Vorobieff, P. & Ecke, R. E. 1998 Vortex structure in rotating Rayleigh–Bénard convection. *Physica* D **123**, 153–160.

Vorobieff, P. & Ecke, R. E. 2002 Turbulent rotating convection: an experimental study. *J. Fluid Mech.* **458**, 191–218.

Xi, H. D., Zhou, Q. & Xia, K. Q. 2006 Azimuthal motion of the mean wind in turbulent thermal convestion. *Phys. Rev.* E **73**, 056312.

Xi, H.-D., Zhou, S.-Q., Zhou, Q., Chan, T.-S. & Xia, K.-Q. 2009 Origin of the temperature oscillation in turbulent thermal convection. *Phys. Rev. Lett.* **102**, 044503.

Xia, K.-Q. 2007 Two clocks for a single engine in turbulent convection. *J. Stat. Mech.* **2007**, N11001.

Xia, K.-Q., Lam, S. & Zhou, S. Q. 2002 Heat-flux measurement in high-Prandtl-number turbulent Rayleigh–Bénard convection. *Phys. Rev. Lett.* **88**, 064501.

Zhong, F., Ecke, R. & Steinberg, V. 1993 Rotating Rayleigh–Bénard convection: asymmetric modes and vortex states. *J. Fluid Mech.* **249**, 135–159.

Zhong, J.-Q., Stevens, R., Clercx, H., Verzicco, R., Lohse, D. & Ahlers, G. 2009 Prandtl-, Rayleigh-, and Rossby-number dependence of heat transport in turbulent rotating Rayleigh–Bénard convection. *Phys. Rev. Lett.* **102**, 044502.

Zhou, Q., Xi, H.-D., Zhou, S.-Q., Sun, C. & Xia, K.-Q. 2009 Oscillations of the large-scale circulation in turbulent Rayleigh–Bénard convection: the sloshing mode and its relationship with the torsional mode. *J. Fluid Mech.* **630**, 367–390.

Zhou, Q. & Xia, K.-Q. 2010 Measured instantaneous viscous boundary layer in turbulent Rayleigh–Bénard convection. *Phys. Rev. Lett.* **104**, 104301.